nature communications

Article

https://doi.org/10.1038/s41467-026-69844-9

# Structural and dynamic insights into agonist recognition and function of the thromboxane $A_2$ receptor

Received: 4 October 2024

Accepted: 11 February 2026

Published online: 23 February 2026

Check for updates

Pawel Krawinski[1,7], Donna Matzov[2,7], Aoife Ryder[1], Kanhaya Lal[3], Dmitry S. Karlov[3], Georges Chalhoub[4,5], Eamon P. Mulvaney[6], B. Therese Kinsella[6], Peter J. McCormick[4,5], Martin Caffrey[1] ✉, Irina G. Tikhonova[3] ✉ & Moran Shalev-Benami[2] ✉

The thromboxane $A_2$ receptor (TP), expressed in platelets and smooth muscle, plays an important role in blood clotting and muscle contraction. The endogenous ligand of this G protein-coupled receptor (GPCR), thromboxane $A_2$ ($TXA_2$), is a short-lived arachidonic acid metabolite with a half-life of ~30 seconds, which makes investigating the TP structure and activation mechanism highly challenging. Here we determine the structures of the TP in complex with the synthetic agonists, U46619 and I-BOP, stable analogues of the natural ligand, in the presence of the signalling protein partner, $G_q$. The structures reveal a unique activation switch for the receptor that differs from typical class A GPCR family members. Complemented by functional studies, mutational analysis, docking, and molecular dynamics (MD) simulations, our investigation highlights the differences between agonist and antagonist binding and explores the ligand entry mechanism to the binding pocket from within the membrane via a molecular gate composed of two transmembrane helices. In addition, our study provides crucial information to aid in the rational design of compounds targeting the TP, and offers mechanistic insights into inherited disorders associated with mutations in the TP.

The thromboxane (TX) $A_2$ receptor (TP) mediates signalling of the prostanoid thromboxane $A_2$ ($TXA_2$) and other endogenous ligands to regulate diverse physiological and pathological processes, including platelet aggregation and smooth muscle cell (SMC) contraction[1–4]. The TP is increasingly being recognized to mediate a myriad of other *pro*-inflammatory, *pro*-mitogenic, and *pro*-fibrotic effects in multiple organ systems[3–5]. The receptor is expressed in many cell types, including platelets, SMCs of the vasculature and pulmonary systems, in endothelial cells, cardiomyocytes, monocytes, and macrophages. TP expression is elevated in several pathological conditions, such as cardiovascular and cardiopulmonary diseases[6–13], as well as in certain cancers[14,15]. Accordingly, the TP is an emerging target for clinical development across multiple indications, which include pulmonary arterial hypertension (PAH)[16–19], idiopathic pulmonary fibrosis[20], and related cardiopulmonary conditions[21,22].

[1]School of Medicine and School of Biochemistry and Immunology, Trinity College Dublin, Dublin, Ireland. [2]Department of Chemical and Structural Biology, Weizmann Institute of Science, Rehovot, Israel. [3]School of Pharmacy, Queen's University Belfast, Belfast, UK. [4]Department of Pharmacology and Therapeutics, University of Liverpool, Institute of Systems, Molecular and Integrative Biology, Sherrington Building, Liverpool, UK. [5]Centre for Endocrinology, William Harvey Research Institute, Barts and the London School of Medicine, Queen Mary, University of London, London, UK. [6]ATXA Therapeutics Limited, UCD Conway Institute of Biomolecular and Biomedical Research, University College Dublin, Belfield, Ireland. [7]These authors contributed equally: Pawel Krawinski, Donna Matzov. ✉e-mail: martin.caffrey@tcd.ie; i.tikhonova@qub.ac.uk; moransb@weizmann.ac.il

The TP is a G protein-coupled receptor (GPCR) of the prostanoid receptor subfamily in the class A GPCR family. In humans, two isoforms, referred to as TPα and TPβ, exist, share the same first 328 amino acids and differ in their carboxyl-terminal tails[23–25]. While TPα and TPβ exhibit similar ligand binding and primary heterotrimeric G protein and effector coupling specificities, they have distinct modes of desensitization[12,23]. As their primary signalling pathway[5,23,26–30], TPα and TPβ identically couple with members of the $G_q$ family, where TP stimulation leads to phospholipase (PL)C-β-mediated phosphoinositide hydrolysis, the liberation of inositol 1,4,5-trisphosphate ($IP_3$) and diacylglycerol (DAG), and the subsequent release of intracellular calcium and activation of protein kinase (PK)C, respectively, for downstream signalling[26–29].

Following the determination of the structure of the inactive TP in complex with the antagonists ramatroban and daltroban in 2019[30], the last few years have witnessed the elucidation of a number of high-resolution prostanoid receptor structures. These include active complexes involving $PGE_2$ receptors (EP2, EP3, and EP4 isoforms)[31–33], the $PGF_{2\alpha}$ receptor (FP)[34], as well as the prostacyclin/$PGI_2$ receptor (IP)[35]. Relatedly, while the current study was being finalized, a structure of TPα-$G_q$ in complex with U46619 was published[36]. Collectively, these structures offer insights into the mechanisms of ligand recognition and G protein coupling within the prostanoid receptor subfamily. Despite these advances, the molecular details underlying agonist recognition by the TP and the structural basis of its activation and G protein coupling remain incomplete[36]. In particular, the question of selectivity and potency is not explained. This deficit in knowledge on TP ligand recognition not only hampers the design of highly selective and high-affinity ligands as therapeutic agents, but it also limits our understanding of the physiological and pathological roles of this clinically-important drug target.

In the current study, we report the cryogenic electron microscopy (cryo-EM) structures of the TPα-$G_q$ complex bound to two potent and specific $TXA_2$ mimetics, U46619 and I-BOP. Complemented by functional, mutational, docking, and molecular dynamics (MD) simulations, these structures reveal a mechanism by which agonists selectively engage with and activate the TP, and how outside-in signalling occurs across the membrane through the receptor to its $G_q$ binding partner. In addition, comparisons with antagonist-bound TP structures identify features distinguishing agonist from antagonist binding, and the differences in conformations that influence receptor activation. Finally, our findings also provide mechanistic insights into inherited disorders associated with mutations in the TP.

## Results and discussion

### Cryo-EM structure determination

For structural studies, the full-length human TPα was cloned into a vector encoding an N-terminal haemagglutinin (HA) signal peptide followed by a cleavable FLAG epitope tag. The receptor was coupled to a mini-$G_{\alpha s/q}$ chimera in which the specificity determinants of the α5 helix of $G_{\alpha q}$ were grafted onto mini-$G_{\alpha s}$. A similar construct has been successfully used for the structure determination of the thyrotropin-release hormone receptor 1 (TRH1R)[37], the 5-hydroxytryptamine receptor 2A (H5T2R)[38], and the galanin receptor type 2 (GAL2R)[39]. The first 36 residues of mini-$G_{\alpha q}$ were replaced by the 30 N-terminal amino acids of $G_{\alpha i2}$ to provide a recognition epitope for scFv16 previously shown to stabilize G protein heterotrimer formation[40]. $TXA_2$, the endogenous ligand for the TP, is chemically unstable with a physiological half-life of only 30 seconds[23], which precludes its use in structural determinations and functional studies. The two agonists used in this investigation, U46619 and I-BOP, are both stable $TXA_2$ mimetics, with high specificity and potency at the TP ($EC_{50}$: 11.22 nM and 1.79 nM for U46619 and I-BOP, respectively; Fig. 1). These agonists were introduced to membranes overexpressing the receptor and the $G_q$ heterotrimer. ScFv16 was later added for further complex stabilization. Through cryo-EM, three-dimensional reconstructions were obtained with nominal resolutions of 3.26 Å and 3.25 Å for complexes with U46619 (TP-U46619) and I-BOP (TP-I-BOP), respectively (Fig. 1, Supplementary Figs. 1–2, and Supplementary Table 1). The EM maps revealed the architecture of all complex components including the

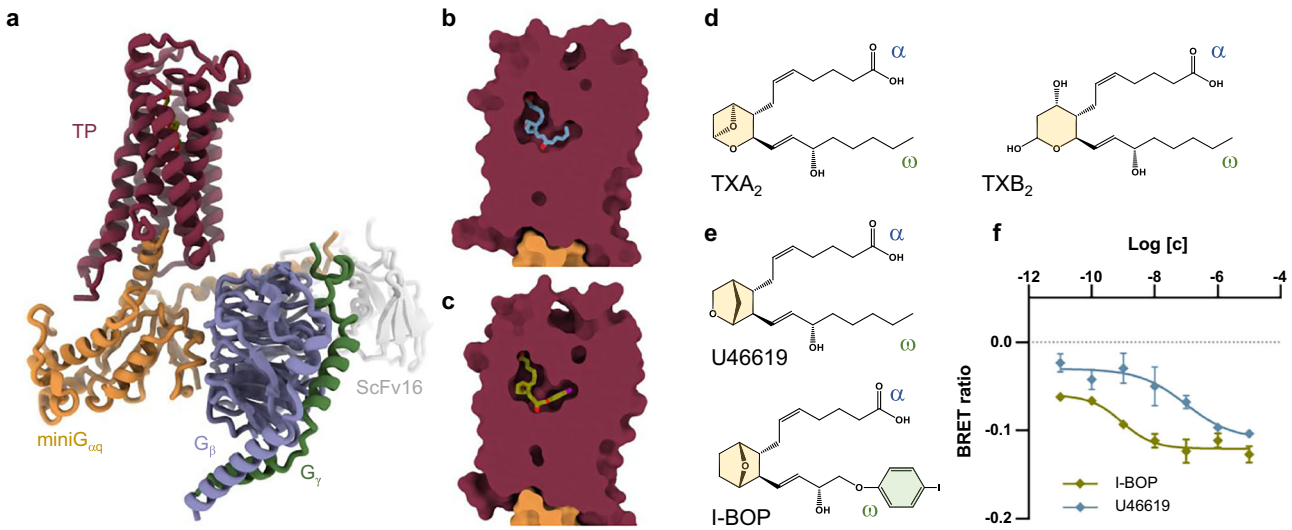


**Fig. 1 | Active state structures and functional characterization of the TP.** **a** Cartoon representation of the active TP structures bound to the agonist I-BOP and the mini-$G_q$ heterotrimer. The TP is coloured dark red, with mini-$G_{\alpha q}$ in gold, $G_\beta$ and $G_\gamma$ in purple and green, respectively, and scFv16 in light grey. I-BOP is in olive green. Cutaway view of the U46619 (**b**, blue) and I-BOP (**c**, green) bound TP structures indicating that both ligands adopt an L-shaped conformation, while occupying a binding pocket that is buried deep within the receptor's transmembrane core. The sealed cavity is proposed to protect the ligands from decomposition by hydration to the water-soluble $TXB_2$. **d** Chemical structures of the endogenous TP agonist $TXA_2$ (left) and its derivative $TXB_2$ (right). **e** Chemical structures of the synthetic agonists used in this study: U46619 and I-BOP. In (**d**) and (**e**), the α- and ω-chains are labelled, the bicyclic ring that differs between the synthetic agonists and the endogenous $TXA_2$ is in yellow, and the iodobenzene group present in I-BOP is in green. **f** $G_q$ heterotrimer dissociation as measured by a loss of BRET after TP stimulation with U46619 (blue) or I-BOP (green) in HEK293 cells transiently co-expressing the wild-type receptor and TRUPATH biosensors for the full-length $G_q$ protein. Data are represented as mean ± SEM from 8 independent experiments for U46619 and 4 independent experiments for I-BOP, performed in triplicate, indicating $EC_{50}$ values of 11.22 ± 5.29 nM and 1.79 ± 1.08 nM (mean ± SEM) for U46619 and I-BOP, respectively.

mode of receptor engagement with the $G_q$ heterotrimer and its ligand binding (Fig. 1).

### TP-$G_q$ complex architecture

The structures of the TP-$G_q$ complex bound to I-BOP and U46619 are highly similar, with an all-atom root mean square deviation (RMSD) of 0.5 Å (Supplementary Fig. 2c). In both structures, the receptor adopts an active state conformation, as evidenced by the outward positioning of transmembrane helix 6 (TM6), which allows for engagement with the $G_\alpha$ subunit (Fig. 1a). A notable feature of the TP is extracellular loop 2 (ECL2), consisting of the highly conserved Pro-Gly-Thr-Trp-Cys-Phe-Ile (PGTWCFI) motif, which creates a rigid lid that limits access of ligands to the orthosteric pocket from the extracellular milieu (Fig. 1b, c and Supplementary Figs. 2d, e and 3a). This feature is also found in other prostanoid and lipid GPCRs and is consistent with previous studies suggesting that ligand entry to these receptors occurs predominantly from the membrane[41].

### Ligand-receptor interactions

Like $TXA_2$, U46619 and I-BOP, have a molecular structure consisting of a centrally-located bicyclic ring with monoenoic (α-chain) and alkyl chain (ω-chain) modifications (Fig. 1d). The α-chain is capped by a carboxyl group, while the ω-chain contains a hydroxyl group and has a terminus that varies from a methyl to more complex ring-containing moieties. Within the ligand-binding pocket, both U46619 and I-BOP assume similar L-shaped conformations, bent at the hydroxyl group, with the extremities of the two chains fixed in position (Figs. 1b, c and 2a).

The carboxylic acid group of the α-chain in U46619 and I-BOP forms polar interactions with residues in TM2, TM7, and ECL2. Both agonists are held firmly in place by $H89^{2.65}$ (Ballesteros–Weinstein numbering) and $R295^{7.40}$ at the carboxylate (Fig. 2c, d). In our BRET signalling assays, an $R295^{7.40}F$ mutation reduced agonist potency ~200-fold, confirming the importance of the polar interaction between $R295^{7.40}$ and the agonists (Fig. 2b and Supplementary Fig. 4). Constant pH simulations indicated that $H89^{2.65}$ is positively charged in its environment, contributing to additional stabilization of the carboxylate (Supplementary Fig. 5). Accordingly, $H89^{2.65}Y/F$ mutations abolished activity, while $H89^{2.65}R/Q$ had less impact, suggesting that $H89^{2.65}$ enables key hydrogen bonding (Fig. 2b and Supplementary Fig. 4). For U46619, an additional hydrogen bond is formed between the carboxylate group and $S181^{ECL2}$ (Fig. 2c). The $TM7^{7.40}$ position is a highly conserved arginine in prostanoid receptors, whereas the S181 ECL2-equivalent is either serine or threonine. This conservancy suggests a common role for residues at these positions in interacting with the carboxyl moiety in most prostanoids through polar contacts (Supplementary Fig. 3b). In contrast, the 2.65 position is uniquely a histidine in the TP. The α-chain of U46619 and I-BOP is further stabilized by a number of hydrophobic contacts with $A31^{1.39}$, $T81^{2.57}$, $V85^{2.61}$, $M112^{3.32}$, $P179^{ECL2}$, $W182^{ECL2}$, $L291^{7.36}$, $L294^{7.39}$, and $T298^{7.43}$ (Fig. 2c, d). With the exception of $A31^{1.39}$ and $T81^{2.57}$, these positions are mostly conserved in other prostanoid receptors and are in accordance with the similarity of the prostanoid ligands that target them (Supplementary Fig. 3b, c). To evaluate the contribution of hydrophobic interactions to prostanoid activity, we designed two loss-of-function mutations, $W182^{ECL2}A$ and $L291^{7.36}A$, and tested the receptor's ability to signal (Fig. 2b and Supplementary Fig. 4). As expected, both mutants were inactive, pointing to the need for large apolar residues at these positions.

The bicyclic rings of U46619 and I-BOP differ from one another in the location of an oxygen atom, which gives rise to an oxane-cyclopentane ring in U46619 and a cyclohexane-oxolane ring in I-BOP (Figs. 1e and 2a). These further differ from the bicyclic oxane-oxetane ring of the endogenous agonist, $TXA_2$ (Fig. 1d). Although no hydrogen bonds are observed between this oxygen and the receptor in either structure, water-mediated interactions occur between the bicyclic ring oxygen and $T298^{7.43}$ in the course of MD simulations performed for both the endogenous and synthetic agonists (Fig. 2f–h and Supplementary Figs. 6 and 7). Accordingly, in our BRET assays, the $T298^{7.43}V$ mutant loses activity, likely due to a lack of hydrogen bond formation (Fig. 2b and Supplementary Fig. 4). Apart from position 7.43, the subpocket surrounding the bicyclic ring in the TP is mostly hydrophobic with $A31^{1.39}$, $F34^{1.42}$, $C35^{1.43}$, $L78^{2.54}$, $T81^{2.57}$, $G82^{2.58}$, and $V85^{2.61}$, collectively creating an apolar environment. This characteristic is unique to the TP and is consistent with the lack of hydroxyl or carbonyl groups on the ring in $TXA_2$, which, in contrast to other endogenous prostanoid GPCR agonists, is quite apolar (Supplementary Fig. 3c).

The central ring in prostaglandins is the main feature that distinguishes endogenous prostanoid GPCR agonists from one another, making it an expected determinant of agonist specificity. Accordingly, sequence alignment revealed substantial differences in the residues constituting the ring-binding subpockets of the members of this receptor subfamily (Supplementary Fig. 3c). Collectively, compared to the residues within the TP, in other prostanoid receptors, the corresponding positions are often polar. For example, the residue at position 2.54 is polar in all prostanoid receptors except the TP, where $L78^{2.54}$ is present. Accordingly, in our BRET assay, the $L78^{2.58}Q$ mutant showed no activation of $G_q$ signalling, suggesting that the hydrophobicity and/or size of the ring-binding subpocket in the TP is important for agonist binding (Fig. 2b and Supplementary Fig. 4).

The ω-chain of U46619 and I-BOP sits in an apolar subpocket located deep inside the receptor where it forms hydrophobic contacts with $L78^{2.54}$, $M112^{3.32}$, $F115^{3.35}$, $G116^{3.36}$, $F184^{ECL2}$, $F200^{5.43}$, $W258^{6.48}$, $L261^{6.51}$, $L294^{7.39}$, and $T298^{7.43}$. Similar residues were also found in other prostanoid GPCRs (Supplementary Fig. 3d). I-BOP sits deeper in the pocket, especially in the region extending from the ring to the ω-chain hydroxyl group (Fig. 2e). This likely arises, in part, because the ω-chain of U46619, which is composed of methylenes, is more flexible than the rigid ω-chain of I-BOP, which ends with an iodobenzene moiety. The iodobenzene makes closer contacts with $F200^{5.43}$, $W258^{6.48}$, and $L261^{6.51}$. This may contribute to the greater affinity TP has for I-BOP compared with U46619 (Fig. 1e).

Collectively, $M112^{3.32}$ and $L294^{7.39}$ form significant hydrophobic contacts with both the α and ω chains of the two agonists. By so doing, they may play a role in stabilizing the agonists' L-shaped conformation, which is presumably required for activity. Evidence supporting this proposal was obtained with the $M112^{3.32}L/L294^{7.39}M$ double mutant and $M112^{3.32}F$ and $L294^{7.39}F$ single mutants, which showed little activity in our BRET assays (Fig. 2b and Supplementary Fig. 4). The corresponding residues in other prostanoid receptors are also mostly conserved (Supplementary Fig. 3b).

### Comparing agonist and antagonist binding to TP

The X-ray structure of the TP in its inactive form bound to the non-prostanoid antagonists, ramatroban and daltroban, was published in 2019[30]. These antagonists adopt an L-shaped configuration in the inactive receptor similar to that observed for the two agonists in the active TP structures reported in this study (Fig. 3a, b). Notably, the overall length of the agonists exceeds that of the antagonists. The α- and ω-chains of the antagonist interact with the binding pocket similarly to agonists. However, additional hydrogen bonds form between the ω-chain sulphonamide in ramatroban and the backbone of $L78^{2.54}$ and the hydroxyl group of $T81^{2.57}$, contributing to placing the antagonist higher in the pocket compared to the agonists (Fig. 3c). These differences in ligand positioning lead to a modified network of interactions with receptor residues that give rise to their differential effects on the receptor. An in-depth description of these interactions and their respective mechanistic implications is provided below.

At the receptor level, the most notable structural rearrangements upon activation include the movement of the extracellular half of TM1 toward TM7, the outward shift of the intracellular half of TM6, and a

https://doi.org/10.1038/s41467-026-69844-9

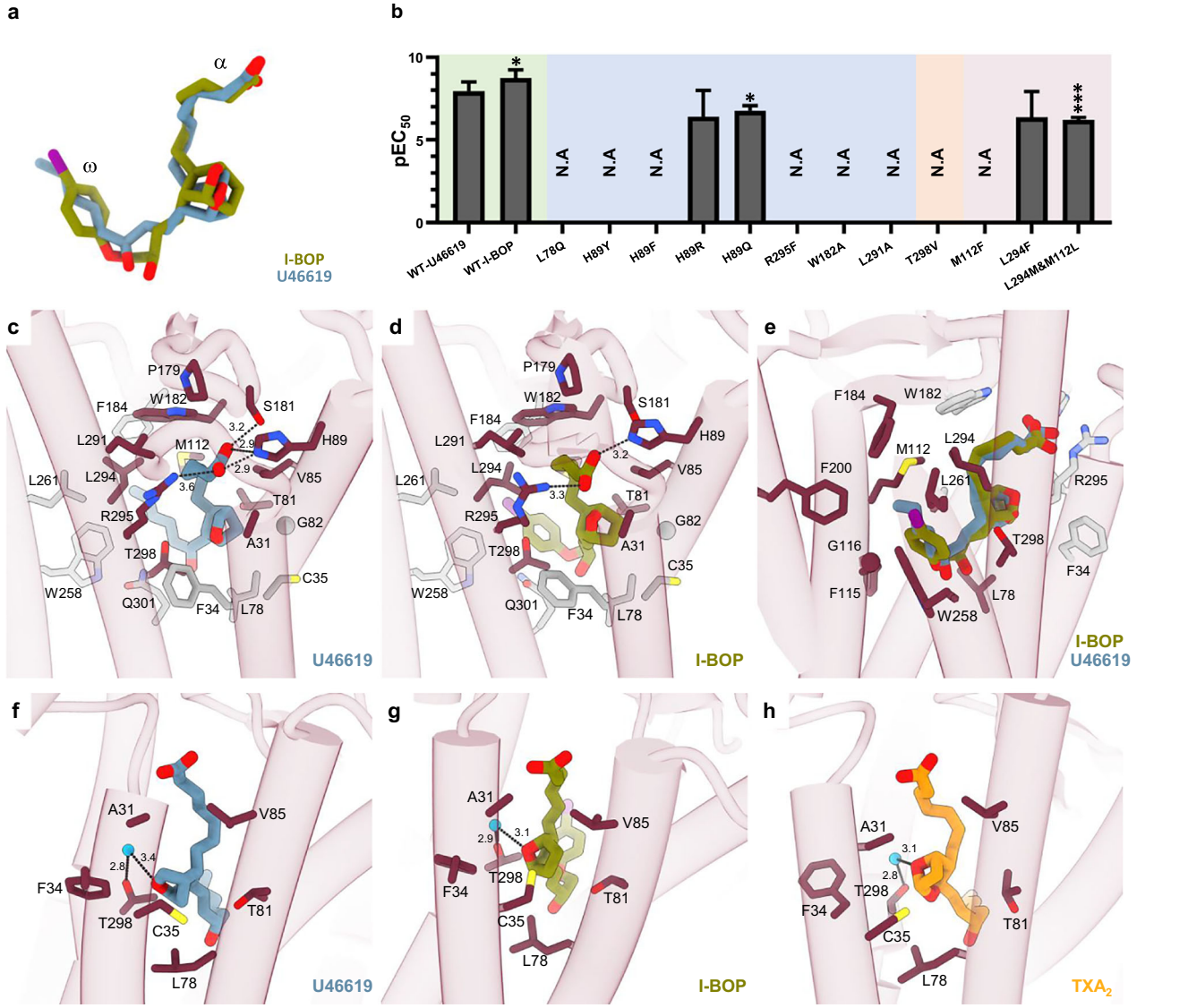


**Fig. 2 | Ligand binding to the TP characterized by cryo-EM, mutational studies, and MD simulations. a** Superposition of U46619 (blue) and I-BOP (green) in the cryo-EM structures. **b** BRET experiments were performed as above and $EC_{50}$ values plotted in response to mutations in the TP canonical binding pocket. $EC_{50}$ values are not available for mutants marked with N.A as their data did not fit dose-response curves. Data are presented as mean ± SEM from three independent experiments. * and *** indicate $P < 0.05$ and $P < 0.001$, respectively. Statistical significance was determined by one-way ANOVA followed by Dunnett's post-hoc tests, comparing the mutants treated with U46619 or I-BOP to the corresponding WT treated with U46619 or I-BOP. Shading indicates the following: WT-TP treated with U46619 and I-BOP (green); mutants of residues involved in agonist binding (blue); the $T298^{7.43}$V mutant (peach); and mutants of residues involved in stabilizing the L-shaped agonist conformation (salmon). All mutants were treated with U46619. Residues surrounding the binding pocket of U46619 (**c**) and I-BOP (**d**). Residues are labelled and shown as sticks. All residues within 5 Å of the ligand are shown in grey or dark red. Residues that are discussed in the main text are highlighted in dark red. Dashed lines indicate hydrogen bonds with distances in Å. **e** Superposition of U46619 (blue) and I-BOP (green) in the binding pocket of the TP. Only the TP-U46619 receptor structure is shown for clarity. The ω-chain of I-BOP differs from that of U46619 and the natural agonist where the methylenes are substituted by iodobenzene. As a result, I-BOP sits deeper in the binding pocket when compared to U46619. **f**–**h** Water-mediated interactions, observed through MD simulations, between the bicyclic ring oxygen and $T298^{7.43}$. A more detailed view of the simulation is provided in Supplementary Fig. 6. Simulations are shown for U46619 (**f**, blue), I-BOP (**g**, green), and the endogenous ligand $TXA_2$ (**h**, orange).

rotation of H8 away from TM6 and toward TM1 (Fig. 3d). In addition to these major conformational adjustments, less dramatic structural changes include the outward movement of the cytoplasmic end of TM2 and TM5 and of ICL2, the inward movement of the cytoplasmic end of TM3, and a small shift in the intracellular end of TM1 toward TM2 and away from the receptor core (Supplementary Fig. 8).

### Structural rearrangements that mediate ligand entry

Comparing the structures of the TP in the active and inactive states, a distinctive change at the extracellular face involves TM1 moving towards TM7 (Fig. 3d and Supplementary Fig. 8). In the inactive TP structures, a gap exists between the extracellular ends of TM1 and TM7. Upon agonist binding, this gap closes. In the active complex, $R295^{7.40}$ on TM7 coordinates with the backbone carbonyl oxygen of $I25^{N\text{-term}}$ near the extracellular end of TM1, sealing the gap (Fig. 3d). Similar interactions involving $R295^{7.40}$ have been reported for other prostanoid receptors, such as EP2, EP3 and EP4[32,33,42]. The magnitude of the TM1 movement was found to vary considerably upon activation, with the TP showing the largest movement, followed closely by EP4 (Supplementary Fig. 9a). Notably, the relative movements of TM1 and TM7 have been remarked on for many class A GPCRs that bind hydrophobic ligands, such as the cannabinoid (CB) and sphingosine-1-

https://doi.org/10.1038/s41467-026-69844-9

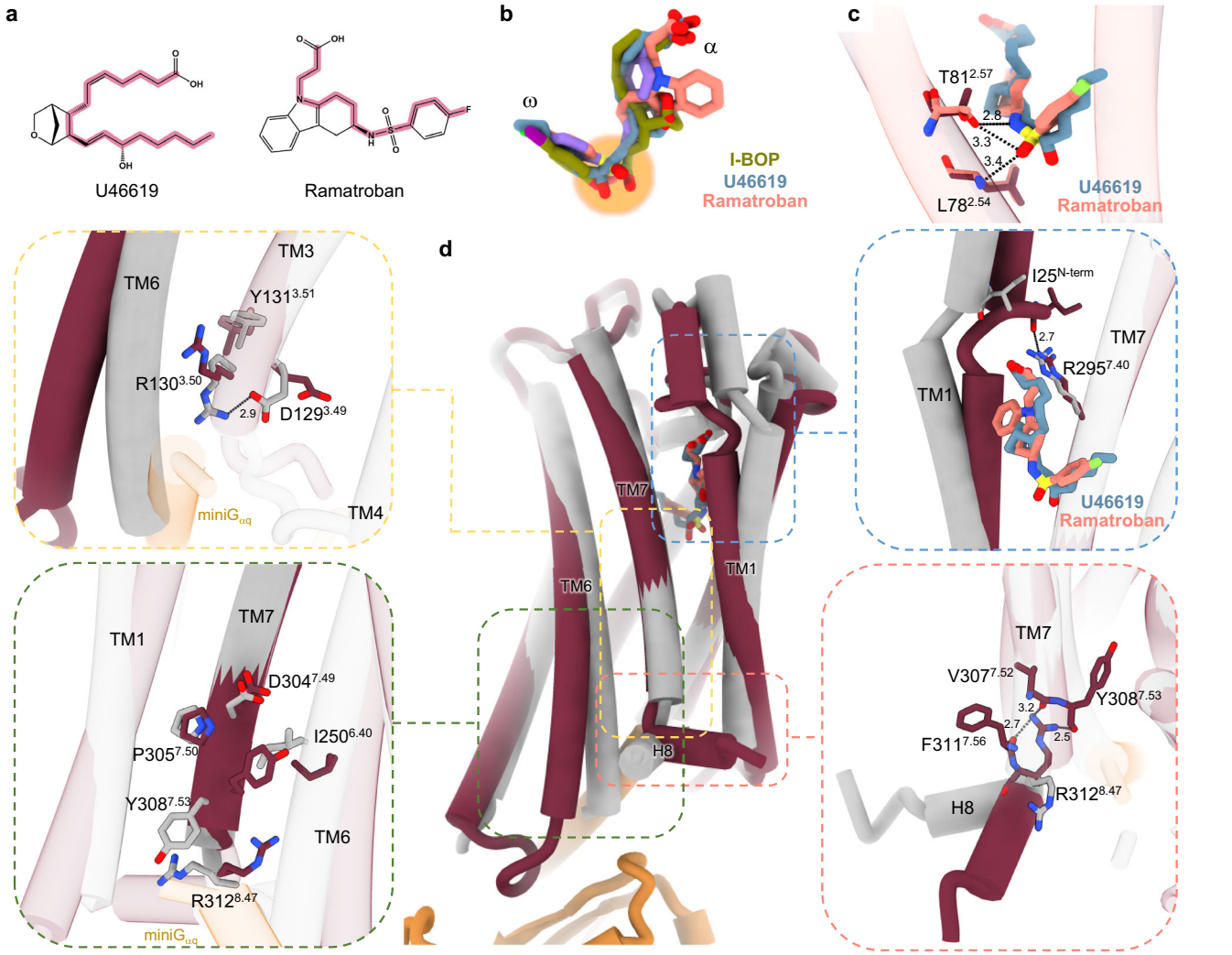


**Fig. 3 | Structural differences in the TP in response to agonist and antagonist binding. a** Chemical structures of the TP agonist, U46619 (left), and antagonist, ramatroban (right). The red outline traces the bonds connecting the carboxyl carbon in the α-chain to the last atom in the ω-chain. There are 16 bonds in the agonist and 14 in the antagonist, indicating that the agonist is the longer ligand. **b** Superposition of the agonists, U46619 (blue) and I-BOP (green), with the antagonist, ramatroban (salmon, PDB 6IIU), indicating that both ligand types adopt an approximate L-shaped conformation in the binding pocket. Agonists sit lower inside the TP binding pocket than antagonists (highlighted by the orange circle). **c** Superposition of U46619 (blue) and ramatroban (salmon, PDB 6IIU) in their respective binding pockets indicates that the antagonist, ramatroban, contacts the hydroxyl group of T81$^{2.57}$ and the backbone of L78$^{2.54}$ through the sulphonamide moiety. Hydrogen bonds are indicated as black dotted lines, with distances in Å. **d** Superposition of the active (dark red) and inactive (grey, PDB 6IIU) TP structures highlighting major structural rearrangements in TM1, TM6, TM7, and H8. Close up views of microswitch residues and residues that undergo large conformational rearrangements are shown in dashed outlines.

phosphate receptors[43,44]. This structural rearrangement is considered to play a role in ligand entry, which happens by way of the membrane, rather than via the extracellular milieu. The gap between TM1 and TM7 is considered to serve as a gate that closes behind the ligand upon entry. Overall, the prostanoid GPCR TM1 movements were greater in magnitude than those for other available inactive/active lipid GPCR structure pairs, such as the CB type 1 ($CB_1$) receptor (Supplementary Fig. 9b). The need for enhanced TM1 flexibility and the ability to seal the binding pocket may relate to the labile nature of endogenous prostanoid agonists, which find a stabilizing environment and longevity in the hydrophobic interior of a closed orthosteric pocket.

To gain a greater understanding of the mechanism by which the extracellular end of TM1 undergoes the open/closed transition for ligand entry, we performed functional assays on TP mutants alongside random accelerated MD (RAMD)[45–47] and supervised MD (suMD) simulations[48–50] (Supplementary Figs. 10 and 11). RAMD examines ligand-receptor dissociation in response to a random directional force, while suMD combines short classical MD simulations with a Tabu-like algorithm, which accepts trajectories when the ligand moves closer to the binding site and rejects them otherwise. Both enhanced sampling methods explore millisecond-scale interactions on nanosecond timeframes. A sequential strategy was employed whereby RAMD was used to study ligand unbinding (computationally efficient but indirect), followed by suMD to examine direct ligand binding, with unbinding results informing ligand placement outside the receptor.

RAMD studies revealed that bulky antagonists (ramatroban and daltroban) primarily dissociated from the receptor via the TM1/TM7 gap, while flexible agonists (U46619 and I-BOP) showed less specific dissociation patterns using both TM1/TM2 and TM1/TM7 openings with considerable frequency and the extracellular route to a lesser extent (Supplementary Fig. 10). These results are consistent with ligand binding to the receptor that is primarily membrane-mediated and are also in agreement with other structures indicating a TM1/TM2 opening that facilitates the entry of lipidic ligands[51]. To avoid bias

toward the open TM1/TM7 gap observed in antagonist-bound states, we simulated I-BOP agonist binding from the membrane using suMD, where the TM1/TM7 gap is closed. Twenty starting structures were selected from 1-µs MD simulations of the agonist- and G protein-free receptor, with I-BOP placed in the membrane extracellular leaflet approximately 45 Å from the binding site. Successful suMD trajectories demonstrated that I-BOP entered the binding site primarily through TM1/TM7 (4 out of 6 simulation runs; Supplementary Fig. 11). Notably, in two independent trajectories, a TM1/TM2 opening was observed, where TM1 moved in an opposite manner to the TM7 gate opening, further highlighting TM1 flexibility and its critical role in membrane-mediated ligand binding (Supplementary Fig. 11).

Interestingly, in both agonist-bound structures, two cholesterol molecules were found docked in a cavity at the extracellular leaflet surface of the receptor created by the closed gap (Supplementary Fig. 12). This cavity is composed mostly of hydrophobic residues in TM1, TM6, and TM7 which include W29$^{1.37}$, F30$^{1.38}$, S33$^{1.41}$, F34$^{1.42}$, V37$^{1.45}$, V253$^{6.43}$, V256$^{6.46}$, C257$^{6.47}$, I292$^{7.37}$, V296$^{7.41}$, W299$^{7.44}$, and L303$^{7.48}$ (Supplementary Fig. 12e). When this gap is open in the inactive receptor, the cavity ceases to exist, and the cholesterol molecules are no longer in evidence at that location. Relatedly, a single cholesterol molecule was reported in each of the inactive structure models. However, these were located in the cytoplasmic membrane leaflet next to the receptor, and they did not overlap with either of the cholesterols in the active TP structures (Supplementary Fig. 12a, b). Two phenylalanines, F30$^{1.38}$ and F34$^{1.42}$, in TM1 undergo major conformational changes upon activation, suggesting that they may function as the hydrophobic gate that closes the TM1/TM7 gap. Superposition with the docked cholesterol molecules further indicates that F30$^{1.38}$ in the inactive state structure clashes with cholesterol localization (Supplementary Fig. 12e, f). Single substitutions of the two phenylalanines to alanine affected the efficacy, but not the potency of receptor activation, while the F34$^{1.42}$Q single mutant had reduced potency (Supplementary Fig. 4). However, the double mutants, F30$^{1.38}$A/F34$^{1.42}$A and F30$^{1.38}$A/F34$^{1.42}$Q were dysfunctional (Supplementary Figs. 4 and 12g). These data provide further experimental evidence supporting the importance of the TM1/TM7 gap in receptor activation, while suggesting that cholesterol may play a role in securing the labile ligand within the pocket.

Interestingly, a W29$^{1.37}$C variant in humans is associated with a rare clotting disorder where uncontrolled bleeding occurs after injury. Specifically, cellular assays have shown reduced surface expression for the mutant receptor, as well as disruptions in ligand binding and receptor activation[52]. W29$^{1.37}$ is a part of the cholesterol binding cavity in the active TP structure (Supplementary Fig. 12e, f). Substitution of the bulky, hydrophobic tryptophan with the smaller, polar cysteine residue may impair receptor association with cholesterol and give rise to membrane localization and signalling defects in individuals harbouring the W29C variant. This proposal is consistent with the important modulatory roles that cholesterol has been shown to play in GPCR function[53,54].

## Rearrangements at the intracellular face and engagement with intracellular partners

The outward movement of the cytoplasmic half of TM6 upon receptor activation is a hallmark of class A GPCRs and is crucial for the opening of the intracellular receptor core for $G_{\alpha q}$ binding and initiation of downstream signalling. Comparing the active and inactive TP structures, TM6 displacement is indeed notable, and is in line with what occurs in other class A GPCRs. In the active TP, this displacement involves the breaking of a conserved ionic lock between E129$^{3.49}$ and R130$^{3.50}$ of the conserved E(D)$^{3.49}$R$^{3.50}$Y$^{3.51}$ motif (Fig. 3d). This triggers a cascade of conformational rearrangements at the intracellular side of the receptor that involves residues in TM5, TM6, TM7, and H8. Specifically, in the inactive structures, residues D238$^{6.28}$, E242$^{6.32}$, and Q246$^{6.36}$ form hydrogen bonds with R317$^{8.52}$, R313$^{8.48}$, and F311$^{7.56}$, respectively. Additionally, R237$^{6.27}$ hydrogen bonds with Y226$^{5.69}$. Most of these polar interactions are lost in the active TP-U46619 structure, except those between E242$^{6.32}$ and R313$^{8.48}$ and between Y226$^{5.69}$ and R237$^{6.27}$. In the TP-I-BOP structure, Q246$^{6.36}$ hydrogen bonds to the backbone carbonyl oxygen of Y308$^{7.53}$, while all of the other aforementioned interactions are lost (Supplementary Fig. 13).

In addition to the TM6 movement, the conserved N(D)$^{7.49}$P$^{7.50}$xxY$^{7.53}$ motif facilitates the inward movement and slight unravelling of the cytoplasmic end of TM7 upon receptor activation. This repositions Y308$^{7.53}$, allowing its side chain to pack against I250$^{6.40}$ in TM6 and freeing R312$^{8.47}$ in H8 to facilitate a clockwise rotation toward TM1 (Fig. 3d). In the inactive state, Y308$^{7.53}$ sterically limits the rotameric freedom of R312$^{8.47}$. The conformational change of Y$^{7.53}$ upon activation is a characteristic of many class A GPCRs. According to our MD simulations, this change is accompanied by major alterations in the water network at the exposed intracellular surface of these receptors (Supplementary Fig. 6).

One of the most notable changes upon TP activation is the 70° rotation of H8 towards the cytoplasmic end of TM1, which is accompanied by a partial unravelling of TM7 and H8 (Fig. 3d). The inactive TP structures, solved by X-ray crystallography, confirm the mechanistic relevance of these changes as H8 is not involved in crystal contacts. The repositioned H8 forms new hydrophobic interactions with TM1 residues, creating a stabilizing interface. The orientation of H8 is secured by a substantial rotation in the side chain of R312$^{8.47}$, enabling it to hydrogen bond with the backbone carbonyl oxygens of V307$^{7.52}$, Y308$^{7.53}$, and F311$^{7.56}$ in the TP-U46619 structure, fastening the base of H8 to TM7. In the TP-I-BOP structure, R312$^{8.47}$ forms polar interactions only with the carbonyl oxygens of V307$^{7.52}$ and Y308$^{7.53}$ (Fig. 3d). To our knowledge, such a large rotation of H8 has not been seen in other class A GPCRs. A similar rotation was observed when the active and inactive EP4 structures were compared, but H8 participated in crystal contacts in the inactive structure of the receptor[32]. Thus, H8 in the TP may act as a key switch by stabilizing TM6 in the inactive state. However, upon receptor activation, the large rotation of H8 enables greater freedom of movement for TM6, allowing TM6 to acquire an active conformation.

## Agonist mediated mechanism of activation

The canonical mechanism of class A GPCR activation includes TM6 relocation for engagement with the α5 helix of $G_{\alpha}$. In many cases, this structural rearrangement involves the ligand contacting a toggle switch composed of a highly conserved tryptophan in TM6 (W$^{6.48}$) and a hydrophobic residue (M/L/F$^{3.36}$) in TM3. In this mechanism, the ligand directly interacts with position 3.36, leading to a shift in the toggle switch, W$^{6.48}$, ultimately causing TM6 movement and receptor activation. In the TP, the residue at 3.36 is G116$^{3.36}$, which because of its size, does not interact with W258$^{6.48}$ in the same way that bulkier residues interact at this position (Fig. 4a). A comparison of the inactive and active TP structures suggests a unique activation mechanism whereby the ω-chain of both U46619 and I-BOP directly contacts W258$^{6.48}$ causing only a small movement of its indole side chain (Fig. 4e). The mechanism further differs from most class A GPCRs, where toggle switch movement is often accompanied by a rearrangement in the P$^{5.50}$I$^{3.40}$F$^{6.44}$ motif, which is absent in the TP, leading to the outward relocation of TM6 and G protein recruitment.

The presence of glycine at position 3.36 is common to many other prostanoid receptors (Supplementary Fig. 3d; DP1, EP1, EP3, FP, and IP), rhodopsins, and other orphan GPCRs (GPR135, GPR149, and GPR160). Previous studies have shown that replacing G$^{3.36}$ in the EP3 receptor with leucine or tryptophan significantly reduced the potency of agonist binding and increased basal activity[41]. Like $TXA_2$, $PGE_2$, the endogenous ligand of EP3, has an extended ω-chain, which supports the claim that this region of the active site is likely to accommodate the

https://doi.org/10.1038/s41467-026-69844-9

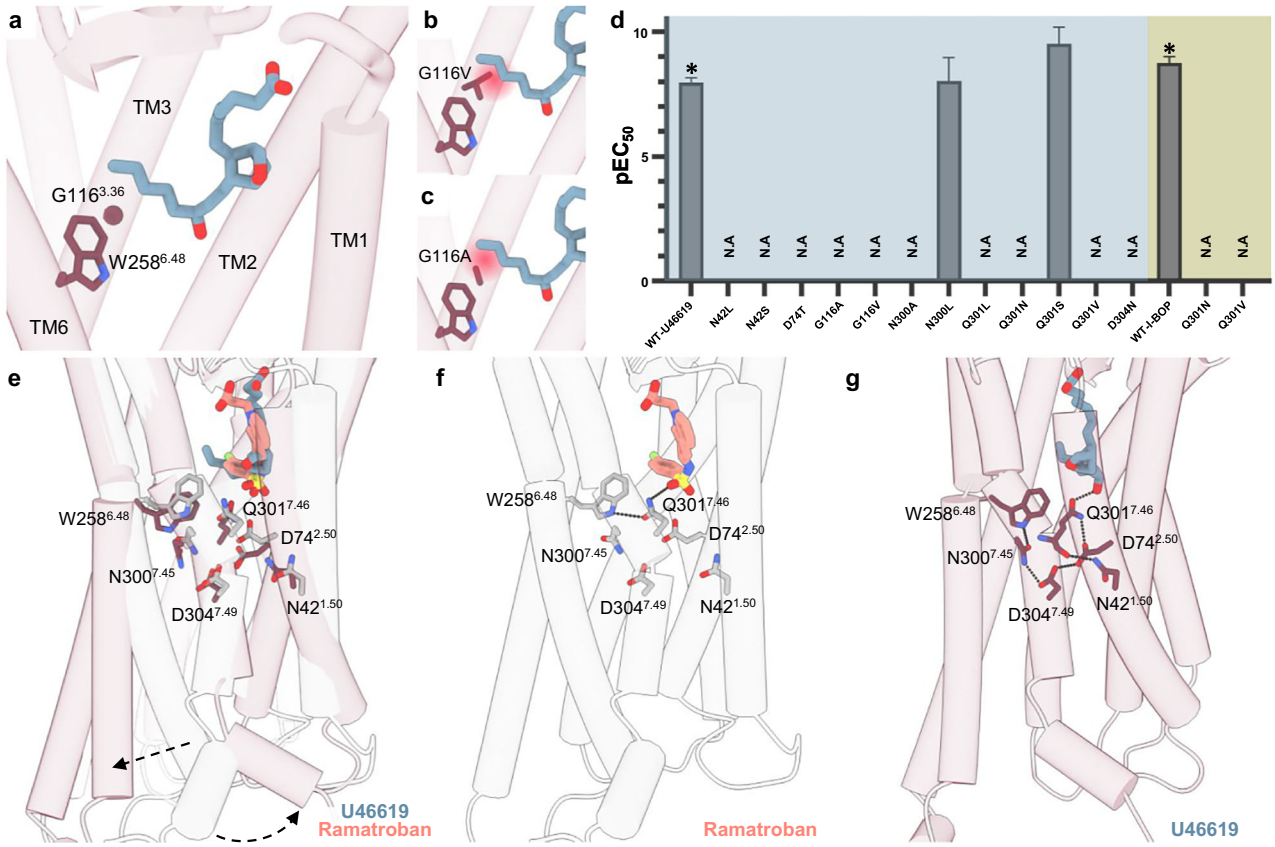


**Fig. 4 | Proposed activation mechanism for the TP. a** U46619 (blue) in the binding pocket of the activated TP, with canonical toggle switch residues highlighted. **b, c** Modelled G116V/A substitutions in the TP sterically clash (red sphere) with the ω-chain of the ligand. **d** $EC_{50}$ values from BRET experiments performed with TP constructs mutated at residues that are part of the proposed activation mechanism. $EC_{50}$ values are not available for mutants marked with N.A as their data did not fit dose-response curves. Data are presented as mean ± SEM from three independent experiments. * indicates $P < 0.05$. Statistical significance was determined by one-way ANOVA followed by Dunnett's post-hoc tests, comparing the mutants treated with U46619 or I-BOP to the corresponding WT treated with U46619 or I-BOP. Shading indicates the following: WT-TP and mutants of residues involved in the activation mechanism treated with U46619 (blue) and I-BOP (green). **e** Superposition of active (dark red) and inactive (grey, PDB 6IIU) TP structures showing conformational changes in the residues involved in receptor activation. **f** The sulphonamide oxygen of ramatroban hydrogen bonds to the side chain amide of $Q301^{7.46}$, which, in turn, enables the carbonyl oxygen to interact with the indole of $W258^{6.48}$. **g** The ω-chain hydroxyl group of U46619 interacts with the carbonyl oxygen of $Q301^{7.46}$, enabling $W258^{6.48}$ to interact with $N300^{7.45}$ and to form an extensive hydrogen bond network with neighbouring residues that drives receptor activation.

ω-chain. Our BRET assay results with the $G116^{3.36}A$ and $G116^{3.36}V$ mutants of TP, which were unable to activate $G_q$ (Fig. 4b–d and Supplementary Fig. 4), support this proposal. This suggests an alternative mechanism of activation where $W258^{6.48}$ movement is auxiliary to, or perhaps unnecessary for, TP activation.

Comparing the inactive and active TP, $N300^{7.45}$ and $Q301^{7.46}$ also undergo significant movements (Fig. 4e). In the agonist-bound structure, the agonists sit lower in the pocket, enabling both residues to relocate relative to their positions in the antagonist-bound form. MD simulations reveal that the hydroxyl group in the ω-chain of both agonists forms a hydrogen bond with the carbonyl oxygen of the $Q301^{7.46}$ amide group, while antagonists form a hydrogen bond with the side chain amide of $Q301^{7.46}$ (Fig. 4f, g and Supplementary Fig. 6). This distinct H-bonding pattern enables the carbonyl group of $Q301^{7.46}$ to interact with the indole NH of $W258^{6.48}$ in the antagonist but not in the agonist complexes. The key difference between agonists and antagonists lies in their capacity to form a hydrogen bond as either a donor (agonists) or acceptor (antagonists) with the amide of $Q301^{7.46}$, which, in turn, alters the interaction of $Q301^{7.46}$ with $W258^{6.48}$. The importance of $Q301^{7.46}$ in TP activation is supported by the $Q301^{7.46}L$, $Q301^{7.46}V$, $Q301^{7.46}S$, and $Q301^{7.46}N$ mutants, none of which, except $Q301^{7.46}S$, showed $G_q$ activation in BRET assays (Fig. 4d and Supplementary Fig. 4). Activity of the $Q301^{7.46}S$ mutant could be due to residue conservation, as other prostanoid receptors have serine at position 7.46 (Supplementary Fig. 3d).

The agonist-induced repositioning of $Q301^{7.46}$ in the TP is accompanied by the formation of a hydrogen bond between $W258^{6.48}$ and $N300^{7.45}$, as inferred from MD simulations. This interaction is not directly visible in the cryo-EM structures. Nevertheless, these residues are in close proximity, supporting the MD findings. Thus, $W258^{6.48}$ adopts inactive or active conformations by interacting with $Q301^{7.46}$ or $N300^{7.45}$, respectively (Fig. 4f, g). Consistent with an integral role played by $N300^{7.45}$ in activation, the $N300^{7.45}A$ mutant was inactive (Fig. 4d and Supplementary Fig. 4). However, $N300^{7.45}L$ was active, which could be due to steric hindrance causing $W258^{6.48}$ to move to the active state. This $W258^{6.48}$-$Q301^{7.46}$-$N300^{7.45}$ rearrangement alters the downward interaction network, enhancing interhelical contacts involving TM7. During activation, protonated $D74^{2.50}$ forms a hydrogen bond with $D304^{7.49}$ of the $D^{7.49}P^{7.50}xxY^{7.53}$ motif, positioning the $Q301^{7.46}$ backbone close to $N42^{1.50}$ thereby enabling hydrogen bond formation (Fig. 4f, g and Supplementary Fig. 6). This draws TM7 closer to TM1, TM2, and TM3, reducing the distance between $G123^{3.43}$ and $Y308^{7.53}$ of the $D^{7.49}P^{7.50}xxY^{7.53}$ motif indicative of activation (Fig. 4e and Supplementary Fig. 6b). Mutating $D74^{2.50}$ to threonine abolished the agonist

response, confirming its key role (Fig. 4d and Supplementary Fig. 4). Position 2.50 is known to interact with ions and is important for GPCR inactivation, being a highly conserved position across class A GPCRs. Accordingly, established disease-associated mutants N42$^{1.50}$S and D304$^{7.49}$N reduced agonist responses 10- to 200-fold, respectively, supporting the importance of this interaction network in activation (Supplementary Fig. 4). The N42$^{1.50}$S TP variant was identified as the first naturally occurring mutant of the highly-conserved N$^{1.50}$ residue in class A GPCRs[55]. A patient with this mutation had significant post-operative and mucocutaneous bleeding, caused by platelet dysfunction due to reduced receptor cell surface expression[55]. A patient with the D304$^{7.49}$N mutation had a history of easy bruising, prolonged epistaxis, and mucocutaneous bleeding, which was attributed to reduced ligand binding to TP[56]. Thus, our structural and mutational data provide a molecular basis for the disorders caused by these mutations.

TM7 side chain rearrangements are coupled to the rotation of H8 upon activation. The movement of TM7 and H8 leads to the untethering of TM6 from these two helices, as hydrogen bonds between Q246$^{6.36}$ and the backbone carbonyl oxygen of F311$^{7.56}$, as well as those between D238$^{6.28}$ and R317$^{8.52}$, are broken. The movements of TM7 and H8 are accompanied by an upward rotation of the side chain of R312$^{8.47}$ on H8, positioning it to hydrogen bond with the backbone carbonyl oxygens of V307$^{7.52}$, Y308$^{7.53}$, and F311$^{7.56}$ in TP-U46619, or with the carbonyl oxygens of V307$^{7.52}$ and Y308$^{7.53}$ in TP-I-BOP. These interactions fix H8 angled toward TM1 in the active state. The attendant loss of the D238$^{6.28}$-R317$^{8.52}$ and Q246$^{6.36}$-F311$^{7.56}$ hydrogen bonds enables the outward movement of TM6. This happens in conjunction with Y308$^{7.53}$ interacting hydrophobically with I250$^{6.40}$, contributing to TM6's outward migration and a rupturing of the strong ionic lock between R130$^{3.50}$ and E240$^{6.30}$. In the TP-I-BOP structure, a further loosening of TM6 from the TM helical core arises from the outward movement of TM5, which breaks the hydrogen bond between Y226$^{5.69}$ and the backbone amino and carbonyl groups of R237$^{6.27}$. These combined movements, triggered by agonist binding and relayed predominantly along TM7, open up the receptor's intracellular groove for engagement with the α5 helix of $G_{\alpha q}$ for subsequent signalling.

## Summary

The structures reported herein reveal the active-state TP bound with two $TXA_2$ mimetics, and in complex with its primary G protein signalling partner, providing unprecedented insights into agonist-receptor-effector interactions. Combined with comparisons to existing antagonist-bound TP complexes, MD simulations, and mutagenesis studies, these structures shed light on the molecular bases of disease-associated TP mutations.

Of particular note, the findings of this study identify a unique GPCR activation mechanism for the TP. Rather than involving the highly-conserved W258$^{6.48}$ toggle switch seen in many class A GPCRs, Q301$^{7.46}$ on TM7 may provide this role in the TP. Antagonists, which serve as hydrogen bond acceptors, do not interact with the carbonyl group of Q301$^{7.46}$, which is free to hydrogen bond to W258$^{6.48}$ and stabilize an inactive receptor conformation. Coincident stabilizing contacts between TM3, TM5, TM7, and H8 sequester TM6 to the receptor core, sealing the G protein recruitment site. In contrast, agonists act as hydrogen bond donors, sitting deeper in the binding pocket, which enables them to interact with Q301$^{7.46}$. This severs interaction of Q301$^{7.46}$ with W258$^{6.48}$, facilitating the formation of an extensive hydrogen bond network with residues in TM1, TM2, and TM7. This is accompanied by an unwinding of the intracellular end of TM7, a large rotation of H8, and the breaking of ties securing TM6 to surrounding helices. Consequently, TM6 moves away from the core, opening the α5 binding groove to enable G protein coupling and downstream signalling.

Our structural, mutational, and computational analyses reveal that the TP employs a membrane-mediated ligand entry mechanism facilitated by TM1 flexibility that creates two alternative entry gates for the agonists, namely TM1/TM7 and TM1/TM2. The dynamic TM1/TM7 gating system, regulated by hydrophobic gatekeepers F30$^{1.38}$ and F34$^{1.42}$, works in concert with cholesterol molecules to accommodate and stabilize labile prostanoid ligands in the binding pocket of the receptor. The clinical relevance of this gating mechanism is highlighted by the bleeding disorder-associated W29$^{1.37}$C variant, where potentially disrupted cholesterol interactions compromise receptor function. While the proposed ligand entry mechanism from MD simulations remains speculative, given the uncertainties about the structure/s of the ligand-free receptor, these insights into the unique structural plasticity of TP provide new opportunities for designing selective therapeutics.

## Methods

### Expression of TP-$G_q$

*Spodoptera frugiperda* (Sf9) insect cells (Oxford Expression Technologies, 600100) were infected with TP and $G_q$ P2 baculoviruses at 100x and 50x viral dilutions, respectively. Cells were cultured in ESF921 medium (without FBS and antibiotics) and infected at a density of 4-5 million cells/mL. Co-expression was carried out for 60 h at 27 °C and 130 rpm. Cells were harvested by centrifugation at 4000 × *g* for 15 min and then stored at −70 °C.

### Purification of TP-$G_q$ with U46619 and I-BOP

Approximately 70 grams of wet cell mass were lysed at room temperature (20–22 °C) using lysis buffer containing 20 mM HEPES-NaOH (pH 7.5), 100 mM NaCl, 10 mM $MgCl_2$, 10 μM U46619 or 5 μM I-BOP, 25 mU/mL apyrase, and protease inhibitor cocktail (PIC) containing 1 mM phenylmethylsulfonyl fluoride, 160 μg/mL benzamidine, and 2.5 μg/mL leupeptin. Five millilitres of lysis buffer were used for every 1 g of wet cell mass. After 1 h of lysis under gentle agitation, the mixture was centrifuged at 37,000 × *g* for 30 min at 4 °C. Cell pellets were combined and homogenized at 4 °C in a Dounce homogenizer with solubilization buffer containing 20 mM HEPES-NaOH (pH 7.5), 100 mM NaCl, 10 mM $MgCl_2$, 10 μM U46619 or 5 μM I-BOP, 0.5 %(w/v) laurylmaltose neopentylglycol (LMNG), 0.1 %(w/v) cholesteryl hemisuccinate (CHS), and PIC, using 5 strokes of a loose-fitting pestle followed by 20 strokes of a tight-fitting pestle. Ten millilitres of solubilization buffer were used for every 1 g of membranes. The homogenized membranes were transferred to a beaker, and solubilization was carried out under gentle agitation for 1.5 h at 4 °C. Non-solubilized material was removed by centrifuging the suspension at 37,000 × *g* for 30 min at 4 °C. Clarified supernatants were transferred to a beaker, and 10 mL of pre-equilibrated *anti*-FLAG beads were added. The beads were pre-equilibrated with 3 column volumes (CVs) of wash buffer containing 20 mM HEPES-NaOH (pH 7.5), 100 mM NaCl, 2 mM $MgCl_2$, 10 μM U46619 or 5 μM I-BOP, 0.075 %(w/v) LMNG, 0.004 %(w/v) CHS, and 0.025 %(w/v) glyco-diosgenin (GDN). Binding of the protein to the *anti*-FLAG beads was carried out under gentle agitation for 3 h at 4 °C. Beads were transferred to a gravity column and were washed with 20 CVs of wash buffer at 4 °C. The beads were incubated in the column for 30 min at 4 °C with 2 CVs of elution buffer containing 20 mM HEPES-NaOH (pH 7.5), 100 mM NaCl, 2 mM $MgCl_2$, 10 μM U46619 or 10 μM I-BOP, 0.075 %(w/v) LMNG, 0.004 %(w/v) CHS, 0.025 %(w/v) GDN, and 0.25 mg/mL FLAG peptide. The protein was collected and concentrated at 4 °C in a 100 kDa molecular weight cut-off (MWCO) concentrator to ~0.5 mL. For TP-I-BOP, excess scFv16 at a 1:1.3 molar ratio was added to the protein before concentration and left overnight (~12 h) at 4 °C without agitation to allow for complex formation. The following day, the protein was concentrated as above. The concentrated protein was prepared for size-exclusion chromatography (SEC) by centrifugation at 17,000 × *g* for 10 min at 4 °C. The sample was then loaded onto and run at 4 °C on a Superose 6 10/300 GL column with running buffer containing 20 mM HEPES-NaOH (pH 7.5), 100 mM

NaCl, 2 mM $MgCl_2$, 10 μM U46619 or 10 μM I-BOP, 0.00075 %(w/v) LMNG, 0.00015 %(w/v) CHS, and 0.00025 %(w/v) GDN. Fractions containing the TP-$G_q$-ligand complex were pooled, concentrated in a 100 kDa MWCO concentrator (~10 mg/mL for TP-U46619 and ~14 mg/mL for TP-I-BOP), and used immediately for cryo-EM grid preparation.

### Expression and purification of scFv16

*Trichoplusia ni* (Tni) Hi5 insect cells (Expression Systems, 94-002 F) were infected with scFv16 P2 baculovirus at a 100x viral dilution. Cells were cultured in ESF921 medium (without FBS and antibiotics) and infected at a density of 4–5 million cells/mL. Expression was carried out for 60 h at 27 °C and 130 rpm. The medium, containing the secreted scFv16, was clarified by centrifugation at 4000 × *g* for 15 min at 4 °C and used immediately for purification. The pH of the supernatant was adjusted to 8.2 using 1 M Tris-HCl buffer (pH 8.2) and then supplemented with 1 mM $NiCl_2$, 5 mM $CaCl_2$, and PIC. Upon addition of the reagents, a white precipitate formed. The mixture was left to stir at room temperature for 1 h after which the supernatant containing the scFv16 was clarified by centrifugation at 4000 × *g* for 15 min at 4 °C and then passed through a 0.45 μm filter. Nickel beads, pre-equilibrated with 3 CVs of wash buffer containing 20 mM HEPES-NaOH (pH 7.5), 100 mM NaCl, and 20 mM imidazole-HCl (pH 7.5), were added to the clarified supernatant. Two millilitres of beads were used per litre of medium. Binding of the protein to the nickel beads was carried out under gentle agitation for 3 h at 4 °C. The beads were transferred to a gravity column and washed with 30 CVs of wash buffer at 4 °C. The protein was eluted from the beads with 2 CVs of elution buffer containing 20 mM HEPES-NaOH (pH 7.5), 100 mM NaCl, and 250 mM imidazole-HCl (pH 7.5) at 4 °C. The eluted protein was concentrated at 4 °C in a 3 kDa MWCO concentrator to ~0.5 mL. The concentrated sample was centrifuged at 17,000 × *g* for 10 min at 4 °C and then loaded onto and run at 4 °C on a Superdex 200 Increase 10/300 GL column with running buffer containing 20 mM HEPES-NaOH (pH 7.5) and 100 mM NaCl. Fractions containing the protein were pooled, concentrated in a 3 kDa MWCO concentrator to ~4 mg/mL, and supplemented with 20 %(v/v) glycerol. The protein was aliquoted, flash frozen in liquid nitrogen, and stored at −70 °C.

### Activity assays

The TRUPATH BRET signalling assays of wild-type TP and its mutants were performed as previously described[57,58]. One microgram of TP plasmid, Rluc8-$G_{\alpha q}$, $G_{\beta 1}$, and GFP2-$G_{\gamma 1}$ were transiently co-transfected into Human Embryonic Kidney (HEK293) cells (ATCC, CRL-1573) in tissue culture dishes using polyethyleneimine. Cells were grown in Dulbecco's Modified Eagle Medium (DMEM) supplemented with 10 % (v/v) FBS and 1 %(v/v) penicillin/streptomycin in a humidified incubator at 37 °C with 5 %(v/v) $CO_2$. Twenty-four hours after transfection, cells from the tissue culture dishes were used to seed poly-D-lysine-treated white 96-well assay plates at $0.6 \times 10^5$ cells per well. The transfection was carried out for another 24 h. One hour prior to performing BRET assays, cells were starved by exchanging their FBS-supplemented DMEM for media without FBS. The media from the plates was aspirated, and coelenterazine 400a solution that was diluted in assay buffer (Hanks' Balanced Salt Solution supplemented with 10 %(w/v) BSA) was added to each well at a final concentration of 5 μM. The plate was placed in the CLARIOStar Plus microplate reader (BMG Labtech) at 30 °C, and the cells allowed to equilibrate with the coelenterazine 400a solution for ~10 min before adding U46619 or I-BOP to the wells at a final concentration range of $10^{-11}$–$10^{-5}$ M. The BRET signal was read using 410–480 nm excitation and 515–530 nm emission filters.

### Cryo-EM, model building, and refinement

A volume of 3.5 μL of purified protein sample at 10 mg/mL for TP-U46619 or 14 mg/mL for TP-I-BOP was applied to glow-discharged (90 s, 15 mA, PELCO easiGlow, Ted Pella) holey carbon gold grids (Quantifoil® R1.2/1.3, 300 mesh). The grids were blotted using a Vitrobot Mark IV (FEI) with 3.5 s blotting time at 22 °C in 100 % relative humidity and vitrified in liquid ethane. A total of 8735 and 3212 micrographs were recorded for the TP-U46119 and TP-I-BOP complexes, respectively, on a Titan Krios electron microscope (ThermoFisher Scientific - FEI) operating at 300 kV at a magnification of 105,000-fold and corresponding to a magnified pixel size of 0.8423 Å. The BioQuantum energy filter (Gatan) was operated with an energy slit width of 20 eV. Micrographs were recorded using a K3 direct electron camera (Gatan) with an exposure rate of ~25.5 electrons $Å^{-2}$ $s^{-1}$ and defocus values ranging from −0.8 μm to −2.0 μm. The total exposure time was 1.49 s, and intermediate frames were recorded in 0.033 s intervals, resulting in an accumulated dose of ~38.4 electrons $Å^{-2}$ and a total of 45 frames per micrograph. Automatic data acquisition was done using EPU 3.6 (FEI, ThermoFisher Scientific).

Patch motion correction, CTF estimation, particle picking, 2D classification, ab initio model reconstruction, and heterogeneous refinement were performed in cryoSPARC v4.2.1[59,60]. Homogeneous groups of particles with well-resolved features were refined using the non-uniform refinement algorithm in cryoSPARC. Particle coordinates with their assigned angles were imported into Relion 4.0[61,62] and were subjected to alignment-free 3D classification to enrich for more refined homogeneous particle populations. Selected particles were then transferred back to cryoSPARC and further refined by non-uniform refinement followed by a local refinement focused on the receptor, excluding the micelle and the G proteins, separately. A flowchart describing data processing steps is available in Supplementary Fig. 1. The final map was reconstructed with a total of 216,383 and 242,712 particles for the TP-U46119 and TP-I-BOP complexes, respectively, and has an indicated nominal resolution of 3.26 Å for the TP-U46619 complex and 3.25 Å for the TP-I-BOP complex. The resolution is based on the gold-standard Fourier shell correlation (FSC) using the 0.143 criterion (Supplementary Fig. 2). Angular distribution for particle projections was plotted using cryoSPARC, local resolution was determined using Phenix 1.20.1[63] and was plotted using ChimeraX 1.8[64].

Initial coordinates were generated using the X-ray structure of the inactive TP (PDB code 6IIU[30]). Ligand coordinates and geometry restraints were generated using eLBOW[65]. Models were initially docked into the EM electrostatic potential map using ChimeraX, followed by iterative manual building in Coot 0.9.8.93[66]. The final models were subjected to global refinement and minimization in real space using *phenix.real_space_refine* implemented in Phenix. MolProbity[67] was used to evaluate model geometry. The final refinement parameters are provided in Supplementary Table 1. Structures have been deposited in the Protein Data Bank (PDB) and Electron Microscopy Data Bank (EMDB) databases with accession codes 9GG5/EMD-51324 and 9GGG/EMD-51331 for TP-U46619 and TP-I-BOP, respectively.

### Molecular dynamics simulations

The PDB structures of the TP bound to U46619, I-BOP, ramatroban, and daltroban were prepared using Schrödinger Maestro 2021-3[68]. Missing loops and side chain atoms were added using knowledge-based homology modelling of the Prime module[69,70] with complete amino acid sequences taken from the UniProt database[71]. The added residues were energy minimized using the 3D builder in Maestro. The N- and C-termini of the receptors and the G protein were capped with acetyl and *N*-methyl groups, respectively. The resulting models were validated using the Protein Reports tool in Maestro, and strong steric clashes were removed by geometry minimization. The protonation states of amino acids at pH 7.4 were predicted using the PROPKA 3.1 module in the Protein Preparation workflow of Maestro[72]. Residue H89 was kept protonated in all simulations, while D74 was protonated only in simulations of agonist-bound complexes[73,74] and the empty (without ligand) form of the same complexes.

The input models for MD simulations were prepared using the CHARMM-GUI server[75–83]. Ligand parameter files were created using the

CHARMM-GUI server employing the CHARMM General Force Field to generate topology and parameter files. The receptor was oriented in a membrane using the PPM server within the CHARMM-GUI[84]. The bilayer membrane, with a solvent layer 22.5 Å thick on each side of the membrane, was composed of 9 different lipids including cholesterol (29.5 %); 1-palmitoyl-2-oleoyl-*sn*-glycero-3-phosphocholine, POPC (27.5 %); 1-palmitoyl-2-oleoyl-*sn*-glycero-3-phosphoethanolamine, POPE (15 %); sphingomyelin, PSM (12 %); 1-palmitoyl-2-oleoyl-*sn*-glycero-3-phosphoserine, POPS (11 %); 1-palmitoyl-2-oleoyl-*sn*-glycero-3-phosphoinositol, POPI (2.5 %); 1-palmitoyl-2-lauroyl-*sn*-glycero-3-phosphocholine, PLPC (1.5 %); ceramide (0.5 %); and 1-palmitoyl-2-lauroyl-*sn*-glycero-3-phosphoglycerol, PLPG (0.5 %) as reported in the literature[85]. The system contained 150 mM NaCl as solvent, and the total number of atoms was between 135,000 and 140,000 for receptor-only systems and between 196,000 and 198,000 atoms for receptor-$G_q$ systems.

Minimization, equilibration, and production were carried out using the PMEMD program from the Amber20 package[86] with the CHARMM36m force field[87], and the TIP3P model[88] for membrane lipids, protein, and water, respectively. The non-bonded interaction cut-off was set to 10 Å. Initially, the energy minimization was performed for 10,000 cycles involving 5000 steps of the steepest descent method followed by 5000 steps of the conjugate gradient approach. Restraints were applied to the heavy atoms of the protein and lipids. The systems were first equilibrated in the NVT ensemble for 25 ps with a target temperature at 310 K using the Langevin thermostat[89] and a friction coefficient of 1.0 $ps^{-1}$. This was followed by 15–20 steps of NPT equilibration (with a 1 fs time step) for 10 ns each using the Monte Carlo (MC) barostat[90] to maintain pressure for the membrane systems at 1.0 bar. In the equilibration, the restraint on the heavy atoms was decreased gradually, and in the final step, only the protein backbone was restrained. Production was done using the Langevin thermostat[89] with a friction coefficient of 1.0 $ps^{-1}$ and the MC barostat[90] with a pressure of 1.0 bar and a time step of 2 fs. Each production run was repeated to generate 3 replicas of 1 μs for the empty and ligand-bound receptor systems and 500 ns for the ligand-bound receptor-$G_q$ systems. Simulation snapshots were saved every 10,000 steps.

The results of simulations were analysed using CPPTRAJ from the Amber20 package and MDAnalysis 2.7.0[91,92]. The residue-ligand interaction energy was calculated with the NAMD2 program[93,94] by using the *namdenergy.tcl* script v1.6 for VMD 1.9.3[95]. Calculations were performed using cut-off and switch parameters of 9 Å and 7.5 Å, respectively. Force field parameters were taken from the CHARMM36m parameter files used for the simulations. Energy calculations were performed using 2000 snapshots of each replica.

## Molecular docking

Protein structures were prepared with the protein preparation module, while the structure of the endogenous $TXA_2$ was assessed with the ligand preparation module of the Schrodinger software. I-BOP from the TP-I-BOP complex was selected as the centre of the docking box. Receptor docking grids were generated with the receptor van der Waals radius scaling of 1.0. Docking poses were obtained and evaluated with the Glide program from Maestro[96,97]. The OPLS_2005 force field was used in all calculations.

## Ligand escape

RAMD simulations were performed following best practice, as described[45–47]. A specific branch of GROMACS 2020.5 was used to enable RAMD simulations[98]. Amber topology and equilibrated coordinate files were converted to GROMACS format using ParmEd[99]. For each ligand, 10 independent 5 ns simulations were run with different random seeds. The temperature was set to 310.15 K using the velocity rescaling thermostat. Verlet integration was used for the equations of motion[100]. The neighbour list was updated every 20 steps with a 12 Å cutoff. To avoid an abrupt change to zero at the cutoff distance, van der Waals potential was multiplied by a switch function between 10 Å and 12 Å to reach zero smoothly at the cutoff distance. Long-range electrostatics were handled with PME[101]. Temperature coupling was done with the Nosé-Hoover thermostat[102] using separate coupling groups for protein/ligand, solvent/ions, and lipids. Pressure coupling employed the Parrinello-Rahman barostat[103]. All bonds with hydrogen atoms were constrained with the LINCS algorithm[104]. The 10 simulation snapshots generated for each ligand were used to initiate 100 RAMD simulations (10 snapshots × 10 seeds) with a random force of 585 kJ $mol^{-1}$ $nm^{-1}$ applied to the ligand centre of mass every 50 steps. Simulations were run until the ligand-reference point separation exceeded 50 Å.

## Agonist binding

Supervised MD (suMD) simulations were performed following the protocol of Pavan et al.[105] using the script 1.2a and ACEMD engine provided[106]. Twenty starting structures were prepared by first selecting four random frames from agonist- and G protein-free receptor simulations, with I-BOP placed in the membrane upper (extracellular) leaflet approximately 45 Å from binding site residues ($A32^{1.40}$, $V36^{1.44}$, $F75^{2.51}$, $L79^{2.55}$, $G82^{2.58}$, $V86^{2.62}$, $A90^{2.66}$, $I113^{3.33}$, $G116^{3.36}$, $L117^{3.37}$, $G180^{ECL2}$, $F184^{ECL2}$, $L259^{6.49}$, $I292^{7.37}$, $R295^{7.40}$, $V296^{7.41}$, $W299^{7.44}$, and $I302^{7.47}$). Each structure was then embedded in a POPC membrane, solvated with water, and equilibrated at physiological NaCl concentration for 5 ns. Five frames were randomly selected from each equilibration, yielding 20 simulation systems.

The suMD algorithm monitored the distance between the ligand and binding site centers of mass (CoM) during simulation. Critical distances defining the association process endpoint were set as: opt_dist = 0.5 Å, bound_dist = 0.75 Å, and meta_dist = 1.0 Å. The algorithm executes 150,000-step simulations, accepting trajectories where the average ligand-to-binding site CoM distance decreases and rejecting those where it increases. Accepted simulations continue from the endpoint, while rejected simulations restart from the previous checkpoint. The process terminates when any critical distance threshold is reached.

## Evaluation of H89 protonation state

Constant pH simulations were performed using the Amber20 program complex following recommendations provided in web-based tutorials (https://ambermd.org/tutorials/advanced/tutorial33/). Protein and ligand structures were extracted from initially equilibrated complexes containing water, different lipids, and ions. New structures were constructed using CHARMM-GUI, with the sole difference being the use of POPC as the only lipid to facilitate implementation of the Lipid21 force field[107]. The FF10 force field for proteins was used as recommended; Gaff2, Lipid21, and the TIP3P model were employed to derive parameters for the ligand, 1-palmitoyl-2-oleoyl-sn-glycero-3-phosphocholine, and water, respectively. The default CHARMM-GUI equilibration procedure was followed, with the only exception being the extension of the production simulation by 5 ns, which was then used for a set of predefined pH values: 2.0, 3.0, 4.0, 4.5, 5.0, 5.5, 6.0, 6.5, 7.0, 7.5, 8.0, 8.5, 9.0, 10.0, and 11.0. Each simulation was repeated 3 times to obtain converged $pK_a$ values. In the case of ligand-bound structures, simulations were repeated 6 times to allow better estimation of protonation state populations at pH 8.0, 8.5, and 9.0. The constant pH simulation protocol includes attempts to change the protonation state for every single protonatable residue (Asp, Glu, and His in this case) every 100 steps of simulation. If the flip of the protonation state was successful, an additional 100 steps were performed before the next flip attempt. To compute the probability of a protonation state flip at a particular pH value, a generalized Born implicit solvation model[108] was used. Solvent and ions were stripped, and the mbondi2 radii set[109] was used in the solvation energy computation. Deprotonated state populations at different pH values were extracted from output files and used to build titration curves. There are two additional approximations used in the simulation. First, the estimation of transition probabilities

between different protonation states was computed assuming the protein is surrounded by water without lipids. Second, the ligand was assumed to be deprotonated at all times, which is a reasonable assumption since it forms a salt bridge with R295$^{7.40}$. In this case, the $pK_a$ of the carboxyl group of the ligand is about 2[110].

### Reporting summary

Further information on research design is available in the Nature Portfolio Reporting Summary linked to this article.

## Data availability

All data needed to evaluate the conclusions in the paper are present in the paper and/or the Supplementary Materials. Structures in the paper have been deposited in the Protein Data Bank (PDB) under accession codes 9GG5 (TP-U46619); and 9GGG (TP-I-BOP). The cryo-EM maps have been deposited in the Electron Microscopy Data Bank (EMDB) under accession codes EMD-51324 (TP-U46619); and EMD-51331 (TP-I-BOP). The following previously reported structures were used for structure analysis: 6IIU (TP-ramatroban); 6IIV (TP-daltroban); 7D7M (EP4-$PGE_2$); 5YWY (EP4-ONO-AE3-208); 6N4B ($CB_1$-MDMB-fubinaca); and 5U09 ($CB_1$-taranabant). The source data for the MD simulation protocols are available on the Zenodo repository [https://doi.org/10.5281/zenodo.17848900]. Source data are provided with this paper.

## References


1. Narumiya, S., Sugimoto, Y. & Ushikubi, F. Prostanoid receptors: structures, properties, and functions. *Physiol. Rev.* **79**, 1193–1226 (1999).
2. Smyth, E. M. Thromboxane and the thromboxane receptor in cardiovascular disease. *Clin. Lipidol.* **5**, 209–219 (2010).
3. Narumiya, S. & Furuyashiki, T. Fever, inflammation, pain and beyond: prostanoid receptor research during these 25 years. *FASEB J.* **25**, 813–818 (2011).
4. Bos, C. L., Richel, D. J., Ritsema, T., Peppelenbosch, M. P. & Versteeg, H. H. Prostanoids and prostanoid receptors in signal transduction. *Int. J. Biochem. Cell Biol.* **36**, 1187–1205 (2004).
5. Smyth, E. M., Grosser, T., Wang, M., Yu, Y. & FitzGerald, G. A. Prostanoids in health and disease. *J. Lipid Res.* **50**, S423–S428 (2009).
6. Badimon, L., Vilahur, G., Rocca, B. & Patrono, C. The key contribution of platelet and vascular arachidonic acid metabolism to the pathophysiology of atherothrombosis. *Cardiovasc. Res.* **117**, 2001–2015 (2021).
7. Al-Naamani, N. et al. Prognostic significance of biomarkers in pulmonary arterial hypertension. *Ann. Am. Thorac. Soc.* **13**, 25–30 (2016).
8. Capra, V., Back, M., Angiolillo, D. J., Cattaneo, M. & Sakariassen, K. S. Impact of vascular thromboxane prostanoid receptor activation on hemostasis, thrombosis, oxidative stress, and inflammation. *J. Thromb. Haemost.* **12**, 126–137 (2014).
9. Capra, V. et al. Full and partial agonists of thromboxane prostanoid receptor unveil fine tuning of receptor superactive conformation and G protein activation. *PLoS ONE* **8**, e60475 (2013).
10. Davi, G., Santilli, F. & Vazzana, N. Thromboxane receptors antagonists and/or synthase inhibitors. *Handb. Exp. Pharmacol.* **2012**, 261–286 (2012).
11. Fontana, P., Zufferey, A., Daali, Y. & Reny, J. L. Antiplatelet therapy: targeting the TxA2 pathway. *J. Cardiovasc. Transl. Res.* **7**, 29–38 (2014).
12. Ashton, A. W. Preparing to strike: acute events in signaling by the serpentine receptor for thromboxane A(2). *Pharm. Ther.* **248**, 108478 (2023).
13. West, J. D. et al. Antagonism of the thromboxane-prostanoid receptor is cardioprotective against right ventricular pressure overload. *Pulm. Circ.* **6**, 211–223 (2016).
14. Ekambaram, P., Lambiv, W., Cazzolli, R., Ashton, A. W. & Honn, K. V. The thromboxane synthase and receptor signaling pathway in cancer: an emerging paradigm in cancer progression and metastasis. *Cancer Metastasis Rev.* **30**, 397–408 (2011).
15. Mulvaney, E. P. et al. Expression of the TPalpha and TPbeta isoforms of the thromboxane prostanoid receptor (TP) in prostate cancer: clinical significance and diagnostic potential. *Oncotarget* **7**, 73171–73187 (2016).
16. Mulvaney, E. P. et al. NTP42, a novel antagonist of the thromboxane receptor, attenuates experimentally induced pulmonary arterial hypertension. *BMC Pulm. Med.* **20**, 85 (2020).
17. Mulvaney, E. P. et al. Efficacy of the thromboxane receptor antagonist NTP42 alone, or in combination with sildenafil, in the sugen/hypoxia-induced model of pulmonary arterial hypertension. *Eur. J. Pharm.* **889**, 173658 (2020).
18. Mulvaney, E. P. et al. The thromboxane receptor antagonist NTP42 promotes beneficial adaptation and preserves cardiac function in experimental models of right heart overload. *Front. Cardiovasc. Med.* **9**, 1063967 (2022).
19. Reid, H. M. et al. Evaluation of NTP42, a novel thromboxane receptor antagonist, in a first-in-human phase I clinical trial. *Front. Pharm.* **14**, 1296188 (2023).
20. Suzuki, T. et al. Thromboxane-prostanoid receptor signaling drives persistent fibroblast activation in pulmonary fibrosis. *Am. J. Respir. Crit. Care Med.* **206**, 596–607 (2022).
21. Mitchell, R. et al. Ifetroban reduces coronary artery dysfunction in a mouse model of Duchenne muscular dystrophy. *Am. J. Physiol. Heart Circ. Physiol.* **321**, H52–H58 (2021).
22. Benfaremo, D., Svegliati, S., Paolini, C., Agarbati, S. & Moroncini, G. Systemic sclerosis: from pathophysiology to novel therapeutic approaches. *Biomedicines* **10**, 163 (2022).
23. Kinsella, B. T. Thromboxane A2 signalling in humans: a 'Tail' of two receptors. *Biochem. Soc. Trans.* **29**, 641–654 (2001).
24. Raychowdhury, M. K. et al. Alternative splicing produces a divergent cytoplasmic tail in the human endothelial thromboxane A2 receptor. *J. Biol. Chem.* **269**, 19256–19261 (1994).
25. Raychowdhury, M. K. et al. Alternative splicing produces a divergent cytoplasmic tail in the human endothelial thromboxane A2 receptor. *J. Biol. Chem.* **270**, 7011 (1995).
26. Woodward, D. F., Jones, R. L. & Narumiya, S. International Union of Basic and Clinical Pharmacology. LXXXIII: classification of prostanoid receptors, updating 15 years of progress. *Pharm. Rev.* **63**, 471–538 (2011).
27. Hirata, M. et al. Cloning and expression of cDNA for a human thromboxane A2 receptor. *Nature* **349**, 617–620 (1991).
28. Kinsella, B. T., O'Mahony, D. J. & Fitzgerald, G. A. The human thromboxane A2 receptor alpha isoform (TP alpha) functionally couples to the G proteins Gq and G11 in vivo and is activated by the isoprostane 8-epi prostaglandin F2 alpha. *J. Pharm. Exp. Ther.* **281**, 957–964 (1997).
29. Offermanns, S. Activation of platelet function through G protein-coupled receptors. *Circ. Res.* **99**, 1293–1304 (2006).
30. Fan, H. et al. Structural basis for ligand recognition of the human thromboxane A(2) receptor. *Nat. Chem. Biol.* **15**, 27–33 (2019).
31. Huang, S. M. et al. Single hormone or synthetic agonist induces G(s)/G(i) coupling selectivity of EP receptors via distinct binding modes and propagating paths. *Proc. Natl. Acad. Sci. USA.* **120**, e2216329120 (2023).
32. Nojima, S. et al. Cryo-EM structure of the prostaglandin E receptor EP4 coupled to G protein. *Structure* **29**, 252–260 e256 (2021).
33. Qu, C. et al. Ligand recognition, unconventional activation, and G protein coupling of the prostaglandin E(2) receptor EP2 subtype. *Sci. Adv.* **7**, eabf1268 (2021).
34. Wu, C. et al. Ligand-induced activation and G protein coupling of prostaglandin F(2alpha) receptor. *Nat. Commun.* **14**, 2668 (2023).

35. Wang, J. J. et al. Molecular recognition and activation of the prostacyclin receptor by anti-pulmonary arterial hypertension drugs. *Sci. Adv.* **10**, eadk5184 (2024).
36. Li, X. et al. Structural basis for ligand recognition and activation of the prostanoid receptors. *Cell Rep.* **43**, 113893 (2024).
37. Yang, F. et al. Structural insights into thyrotropin-releasing hormone receptor activation by an endogenous peptide agonist or its orally administered analogue. *Cell Res.* **32**, 858–861 (2022).
38. Kim, K. et al. Structure of a Hallucinogen-Activated Gq-Coupled 5-HT(2A) Serotonin Receptor. *Cell* **182**, 1574–1588 e1519 (2020).
39. Jiang, W. & Zheng, S. Structural insights into galanin receptor signaling. *Proc. Natl. Acad. Sci. USA.* **119**, e2121465119 (2022).
40. Maeda, S. et al. Development of an antibody fragment that stabilizes GPCR/G-protein complexes. *Nat. Commun.* **9**, 3712 (2018).
41. Audet, M. & Stevens, R. C. Emerging structural biology of lipid G protein-coupled receptors. *Protein Sci.* **28**, 292–304 (2019).
42. Audet, M. et al. Crystal structure of misoprostol bound to the labor inducer prostaglandin E(2) receptor. *Nat. Chem. Biol.* **15**, 11–17 (2019).
43. Hua, T. et al. Activation and signaling mechanism revealed by cannabinoid receptor-G(i) complex structures. *Cell* **180**, 655–665 e618 (2020).
44. Yu, L. et al. Structural insights into sphingosine-1-phosphate receptor activation. *Proc. Natl. Acad. Sci. USA.* **119**, e2117716119 (2022).
45. Kokh, D. B., Kaufmann, T., Kister, B. & Wade, R. C. Machine learning analysis of tauRAMD trajectories to decipher molecular determinants of drug-target residence times. *Front. Mol. Biosci.* **6**, 36 (2019).
46. Kokh, D. B. et al. A workflow for exploring ligand dissociation from a macromolecule: efficient random acceleration molecular dynamics simulation and interaction fingerprint analysis of ligand trajectories. *J. Chem. Phys.* **153**, 125102 (2020).
47. Kokh, D. B. et al. Estimation of drug-target residence times by tau-random acceleration molecular dynamics simulations. *J. Chem. Theory Comput.* **14**, 3859–3869 (2018).
48. Sabbadin, D. & Moro, S. Supervised Molecular Dynamics (SuMD) as a helpful tool to depict GPCR–ligand recognition pathway in a nanosecond time scale. *J. Chem. Inf. Model* **54**, 372–376 (2014).
49. Cuzzolin, A. et al. Deciphering the complexity of ligand–protein recognition pathways using supervised molecular dynamics (SuMD) simulations. *J. Chem. Inf. Model.* **56**, 687–705 (2016).
50. Atanasio, S., Deganutti, G. & Reynolds, C. A. Addressing free fatty acid receptor 1 (FFAR1) activation using supervised molecular dynamics. *J. Comput. Aided Mol. Des.* **34**, 1181–1193 (2020).
51. Aranda-García, D. et al. Large scale investigation of GPCR molecular dynamics data uncovers allosteric sites and lateral gateways. *Nat. Commun.* **16**, 2020 (2025).
52. Mumford, A. D. et al. Platelet dysfunction associated with the novel Trp29Cys thromboxane A(2) receptor variant. *J. Thromb. Haemost.* **11**, 547–554 (2013).
53. Jakubik, J. & El-Fakahany, E. E. Allosteric modulation of GPCRs of class A by cholesterol. *Int. J. Mol. Sci.* **22**, 1953 (2021).
54. Paila, Y. D. & Chattopadhyay, A. Membrane cholesterol in the function and organization of G-protein coupled receptors. *Sub Cell. Biochem.* **51**, 439–466 (2010).
55. Nisar, S. P. et al. A novel thromboxane A2 receptor N42S variant results in reduced surface expression and platelet dysfunction. *Thrombosis Haemost.* **111**, 923–932 (2014).
56. Mumford, A. D. et al. A novel thromboxane A2 receptor D304N variant that abrogates ligand binding in a patient with a bleeding diathesis. *Blood* **115**, 363–369 (2010).
57. DiBerto, J. F., Smart, K., Olsen, R. H. J. & Roth, B. L. Agonist and antagonist TRUPATH assays for G protein-coupled receptors. *STAR Protoc.* **3**, 101259 (2022).
58. Olsen, R. H. J. et al. TRUPATH, an open-source biosensor platform for interrogating the GPCR transducerome. *Nat. Chem. Biol.* **16**, 841–849 (2020).
59. Punjani, A., Rubinstein, J. L., Fleet, D. J. & Brubaker, M. A. CryoSPARC: algorithms for rapid unsupervised cryo-EM structure determination. *Nat. Methods* **14**, 290–296 (2017).
60. Punjani, A., Zhang, H. & Fleet, D. J. Non-uniform refinement: adaptive regularization improves single-particle cryo-EM reconstruction. *Nat. Methods* **17**, 1214–1221 (2020).
61. Kimanius, D., Dong, L., Sharov, G., Nakane, T. & Scheres, S. H. W. New tools for automated cryo-EM single-particle analysis in RELION-4.0. *Biochem. J.* **478**, 4169–4185 (2021).
62. Scheres, S. H. Processing of structurally heterogeneous Cryo-EM data in RELION. *Methods Enzymol.* **579**, 125–157 (2016).
63. Afonine, P. V. et al. Real-space refinement in PHENIX for cryo-EM and crystallography. *Acta Crystallogr. D. Struct. Biol.* **74**, 531–544 (2018).
64. Meng, E. C. et al. UCSF ChimeraX: Tools for structure building and analysis. *Protein Sci.* **32**, e4792 (2023).
65. Moriarty, N. W., Grosse-Kunstleve, R. W. & Adams, P. D. electronic Ligand Builder and Optimization Workbench (eLBOW): a tool for ligand coordinate and restraint generation. *Acta Crystallogr. Sect. D. Biol. Crystallogr.* **65**, 1074–1080 (2009).
66. Emsley, P., Lohkamp, B., Scott, W. G. & Cowtan, K. Features and development of Coot. *Acta Crystallogr. Sect. D. Biol. Crystallogr.* **66**, 486–501 (2010).
67. Williams, C. J. et al. MolProbity: more and better reference data for improved all-atom structure validation. *Protein Sci.* **27**, 293–315 (2018).
68. Schrödinger Release 2021-3: Maestro, Schrödinger, LLC, New York, NY, 2021.
69. Jacobson, M. P. et al. A hierarchical approach to all-atom protein loop prediction. *Proteins* **55**, 351–367 (2004).
70. Schrödinger Release 2021-3: Prime, Schrödinger, LLC, New York, NY, 2021.
71. UniProt C UniProt: the Universal Protein Knowledgebase in 2023. *Nucleic Acids Res.* **51**, D523–D531 (2023).
72. Sastry, G. M., Adzhigirey, M., Day, T., Annabhimoju, R. & Sherman, W. Protein and ligand preparation: parameters, protocols, and influence on virtual screening enrichments. *J. Comput. Aided Mol. Des.* **27**, 221–234 (2013).
73. Vickery, O. N. et al. Intracellular transfer of Na(+) in an active-state G-protein-coupled receptor. *Structure* **26**, 171–180 e172 (2018).
74. Zhang, X. C., Sun, K., Zhang, L., Li, X. & Cao, C. GPCR activation: protonation and membrane potential. *Protein Cell* **4**, 747–760 (2013).
75. Brooks, B. R. et al. CHARMM: the biomolecular simulation program. *J. Comput. Chem.* **30**, 1545–1614 (2009).
76. Jo, S., Kim, T. & Im, W. Automated builder and database of protein/membrane complexes for molecular dynamics simulations. *PLoS ONE* **2**, e880 (2007).
77. Jo, S., Kim, T., Iyer, V. G. & Im, W. CHARMM-GUI: a web-based graphical user interface for CHARMM. *J. Comput. Chem.* **29**, 1859–1865 (2008).
78. Jo, S., Lim, J. B., Klauda, J. B. & Im, W. CHARMM-GUI Membrane Builder for mixed bilayers and its application to yeast membranes. *Biophys. J.* **97**, 50–58 (2009).
79. Kim, S. et al. CHARMM-GUI ligand reader and modeler for CHARMM force field generation of small molecules. *J. Comput. Chem.* **38**, 1879–1886 (2017).
80. Lee, J. et al. CHARMM-GUI input generator for NAMD, GROMACS, AMBER, OpenMM, and CHARMM/OpenMM simulations using the CHARMM36 additive force field. *J. Chem. Theory Comput.* **12**, 405–413 (2016).

81. Lee, J. et al. CHARMM-GUI supports the Amber force fields. *J. Chem. Phys.* **153**, 035103 (2020).
82. Lee, J. et al. CHARMM-GUI membrane builder for complex biological membrane simulations with glycolipids and lipoglycans. *J. Chem. Theory Comput.* **15**, 775–786 (2019).
83. Wu, E. L. et al. CHARMM-GUI Membrane Builder toward realistic biological membrane simulations. *J. Comput. Chem.* **35**, 1997–2004 (2014).
84. Lomize, M. A., Pogozheva, I. D., Joo, H., Mosberg, H. I. & Lomize, A. L. OPM database and PPM web server: resources for positioning of proteins in membranes. *Nucleic Acids Res.* **40**, D370–D376 (2012).
85. Green, S. M., Padula, M. P., Marks, D. C. & Johnson, L. The lipid composition of platelets and the impact of storage: an overview. *Transfus. Med. Rev.* **34**, 108–116 (2020).
86. Case, D. A. et al. AMBER 2020. (University of California, San Francisco, 2020).
87. Huang, J. et al. CHARMM36m: an improved force field for folded and intrinsically disordered proteins. *Nat. Methods* **14**, 71–73 (2017).
88. Jorgensen, W. L., Chandrasekhar, J., Madura, J. D., Impey, R. W. & Klein, M. L. Comparison of simple potential functions for simulating liquid water. *J. Chem. Phys.* **79**, 926–935 (1983).
89. Pastor, R. W., Brooks, B. R. & Szabo, A. An analysis of the accuracy of Langevin and molecular dynamics algorithms. *Mol. Phys.* **65**, 1409–1419 (1988).
90. Åqvist, J., Wennerström, P., Nervall, M., Bjelic, S. & Brandsdal, B. O. Molecular dynamics simulations of water and biomolecules with a Monte Carlo constant pressure algorithm. *Chem. Phys. Lett.* **384**, 288–294 (2004).
91. Gowers, R. J. et al. MDAnalysis: A Python package for the rapid analysis of molecular dynamics simulations. In *Proceedings of the 15th Python in Science Conference* (Eds. Benthall, S. & Rostrup, S.) 98–105, (SciPy, Austin, TX, 2016).
92. Michaud-Agrawal, N., Denning, E. J., Woolf, T. B. & Beckstein, O. MDAnalysis: a toolkit for the analysis of molecular dynamics simulations. *J. Comput. Chem.* **32**, 2319–2327 (2011).
93. Phillips, J. C. et al. Scalable molecular dynamics on CPU and GPU architectures with NAMD. *J. Chem. Phys.* **153**, 044130 (2020).
94. Phillips, J. C. et al. Scalable molecular dynamics with NAMD. *J. Comput. Chem.* **26**, 1781–1802 (2005).
95. Humphrey, W., Dalke, A. & Schulten, K. VMD: visual molecular dynamics. *J. Mol. Graph.* **14**, 33–38 (1996).
96. Schrödinger Release 2021-3: Glide, Schrödinger, LLC, New York, NY, 2021.
97. Friesner, R. A. et al. Glide: a new approach for rapid, accurate docking and scoring. 1. Method and assessment of docking accuracy. *J. Med. Chem.* **47**, 1739–1749 (2004).
98. Abraham, M. J., van der Spoel, D., Lindahl, E. & Hess, B. GROMACS: High performance molecular simulations via multi-level parallelism and 1.5-fold faster GPU acceleration. SoftwareX 1–2, 19–25 (2015).
99. Shirts, M. R. et al. Lessons learned from comparing molecular dynamics engines on the SAMPL5 dataset. *J. Comput. Aided Mol. Des.* **31**, 147–161 (2017).
100. Verlet, L. Computer "experiments" on classical fluids. I. Thermodynamic properties of Lennard-Jones molecules. *Phys. Rev.* **159**, 98–103 (1967).
101. Darden, T., York, D. & Pedersen, L. Particle mesh Ewald: an N·log(N) method for Ewald sums in large systems. *J. Chem. Phys.* **98**, 10089–10092 (1993).
102. Evans, D. J. & Holian, B. L. The Nose–Hoover thermostat. *J. Chem. Phys.* **83**, 4069–4074 (1985).
103. Parrinello, M. & Rahman, A. Polymorphic transitions in single crystals: a new molecular dynamics method. *J. Appl. Phys.* **52**, 7182–7190 (1981).
104. Hess, B., Bekker, H., Berendsen, H. J. C. & Fraaije, J. G. E. M. LINCS: a linear constraint solver for molecular simulations. *J. Comput. Chem.* **18**, 1463–1472 (1997).
105. Pavan, M., Bassani, D., Sturlese, M. & Moro, S. Investigating RNA–protein recognition mechanisms through supervised molecular dynamics (SuMD) simulations. *NAR Genom. Bioinformatics* **4**, lqac088 (2022).
106. Harvey, M. J., Giupponi, G. & Fabritiis, G. D. ACEMD: accelerating biomolecular dynamics in the microsecond time scale. *J. Chem. Theory Comput.* **5**, 1632–1639 (2009).
107. Dickson, C. J., Walker, R. C. & Gould, I. R. Lipid21: complex lipid membrane simulations with AMBER. *J. Chem. Theory Comput.* **18**, 1726–1736 (2022).
108. Onufriev, A., Bashford, D. & Case, D. A. Exploring protein native states and large-scale conformational changes with a modified generalized born model. *Proteins* **55**, 383–394 (2004).
109. Nguyen, H., Roe, D. R. & Simmerling, C. Improved generalized born solvent model parameters for protein simulations. *J. Chem. Theory Comput.* **9**, 2020–2034 (2013).
110. Swails, J. M., York, D. M. & Roitberg, A. E. Constant pH replica exchange molecular dynamics in explicit solvent using discrete protonation states: implementation, testing, and validation. *J. Chem. Theory Comput.* **10**, 1341–1352 (2014).


## Acknowledgements

We thank past and present members of the MS&FB group for their assorted contributions to this study. Dr. Nadav Elad is acknowledged for assisting with cryo-EM data collection. The work was supported, in part, by Science Foundation Ireland grants 16/IA/4435 and 22/FFP-A/10278 (M.C.), the European Union's Horizon 2020 research and innovation program under the European Research Council (ERC, grant no. 949364, M.S.-B), the Blavatnik Foundation (M.C. and M.S.-B.), an Irish Research Council Postgraduate Scholarship (GOIPG/2019/3074, P.K), the Zuckerman STEM Leadership Program (M.S.-B.), and the Biotechnology and Biological Sciences Research Council (U.K.) grant BB/R007101/1 (to I.G.T.). This project made use of computational time on Kelvin-2 supported by Engineering and Physical Sciences Research Council (EPSRC) (grant no. EP/T022175/1 and EP/W03204X/1), and ARCHER2 granted via the UK High-End Computing Consortium for Biomolecular Simulation, HECBioSim (https://www.hecbiosim.ac.uk), supported by EPSRC (grant no. EP/R029407/1 and EP/W03204X/1). M.S.-B. holds the Tauro Career Development Chair in Biomedical Research.

## Author contributions

M.C. and M.S.-B devised the original research plan; P.K produced and purified proteins with the assistance of A.R. and P.K. ran BRET assays with the help of G.C. and under the supervision of P.J.M.; P.K. prepared samples for EM with the help of D.M., and under the supervision of M.S.-B.; D.M. prepared grids, obtained cryo-EM data, processed data, and modelled the structure under the supervision of M.S.-B.; MD simulations and docking were performed by K.L. and D.S.K. under the supervision of I.G.T. M.C., I.G.T., P.J.M., and M.S.-B. supervised research; P.K. wrote the original manuscript with the help of M.C. Revised manuscript versions were prepared by P.K., M.C., I.G.T., E.M., B.T.K., and M.S.-B. All authors provided input for the final version of the manuscript.

## Competing interests

The authors declare no competing interests.

## Additional information

**Supplementary information** The online version contains supplementary material available at https://doi.org/10.1038/s41467-026-69844-9.

**Correspondence** and requests for materials should be addressed to Martin Caffrey, Irina G. Tikhonova or Moran Shalev-Benami.

**Peer review information** *Nature Communications* thanks Jia Duan and the other, anonymous, reviewer(s) for their contribution to the peer review of this work. A peer review file is available.

**Reprints and permissions information** is available at http://www.nature.com/reprints

**Publisher's note** Springer Nature remains neutral with regard to jurisdictional claims in published maps and institutional affiliations.

**Open Access** This article is licensed under a Creative Commons Attribution 4.0 International License, which permits use, sharing, adaptation, distribution and reproduction in any medium or format, as long as you give appropriate credit to the original author(s) and the source, provide a link to the Creative Commons licence, and indicate if changes were made. The images or other third party material in this article are included in the article's Creative Commons licence, unless indicated otherwise in a credit line to the material. If material is not included in the article's Creative Commons licence and your intended use is not permitted by statutory regulation or exceeds the permitted use, you will need to obtain permission directly from the copyright holder. To view a copy of this licence, visit http://creativecommons.org/licenses/by/4.0/.

© The Author(s) 2026

## Supplementary Information

# Structural and Dynamic Insights into Agonist Recognition by and Function of the Thromboxane $A_2$ Receptor: Implications for Disease-Causing Mutations

Pawel Krawinski[1†], Donna Matzov[2†], Aoife Ryder[1], Kanhaya Lal[3], Dmitry S. Karlov[3], Georges Chalhoub[4,5], Eamon P. Mulvaney[6], B. Therese Kinsella[6], Peter J. McCormick[4,5], Martin Caffrey[1*], Irina G. Tikhonova[3*], Moran Shalev-Benami[2*]

[1]School of Medicine and School of Biochemistry and Immunology, Trinity College Dublin, Dublin D02 R590, Ireland. [2]Department of Chemical and Structural Biology, Weizmann Institute of Science, Rehovot 7610001, Israel. [3]School of Pharmacy, Queen's University Belfast, Belfast BT9 7BL, UK. [4]Department of Pharmacology and Therapeutics, University of Liverpool, Institute of Systems, Molecular and Integrative Biology, Sherrington Building, Ashton Street, Liverpool L69 3GE, UK. [5]Centre for Endocrinology, William Harvey Research Institute, Barts and the London School of Medicine, Queen Mary, University of London, London, UK. [6]ATXA Therapeutics Limited, UCD Conway Institute of Biomolecular and Biomedical Research, University College Dublin, Belfield, Dublin 4, Ireland.

***Corresponding authors:** martin.caffrey@tcd.ie; i.tikhonova@qub.ac.uk; moransb@weizmann.ac.il

**Supplementary Discussion**

**Supplementary Figures 1-15**

**Supplementary Tables 1-3**

**Supplementary References**

## Supplementary Discussion

### TM1 involvement in the mechanism of receptor activation

In the MD simulation models of the active, agonist-bound states of the thromboxane (TX) $A_2$ receptor (TP), G38$^{1.46}$ forms a hydrogen bond network with N42$^{1.50}$ and Q301$^{7.46}$. N42$^{1.50}$ links TM1 to TM7 by using its amide group to hydrogen bond to the backbone carbonyls of both G38$^{1.46}$ and Q301$^{7.46}$. These interactions likely hold TM1 in the closed conformation. Given that the changes in TM1 conformation possibly happen as a result of agonist binding, the role of the movement of this helix in receptor activation was investigated by BRET assays of the G38$^{1.46}$A, G38$^{1.46}$V, N42$^{1.50}$S, and P28$^{1.36}$C/A90$^{2.66}$C mutants (Supplementary Fig. 4). The G38$^{1.46}$A and G38$^{1.46}$V mutants were unable to activate $G_q$ suggesting that replacing glycine reduces helix flexibility and its ability to act as a hinge point. The N42$^{1.50}$S disease-related mutant negatively impacts the receptor likely due to the loss of hydrogen bonding between G38$^{1.46}$ and Q301$^{7.46}$ in the active TP (a serine is unable to hydrogen bond to both of these residues), and as already discussed, N42$^{1.50}$ is directly involved in the activation mechanism. A rationally designed disulphide bridge between TM1 and TM2 in the P28$^{1.36}$C/A90$^{2.66}$C double mutant, aimed at preventing TM1 movement, resulted in reduced agonist efficacy. These mutagenesis data strongly suggest that TM1 movement is necessary for receptor activation.

### Voltage-dependent modulation

Voltage-dependent modulation is often neglected as a means for regulating receptor function. Changes in polarization state happen in most cells including platelets and not just those of excitable tissue such as neurons, and cardiac and smooth muscle. Of the receptors investigated in a recent study[1], the TP proved to be particularly sensitive. R295$^{7.40}$, which plays a key role in binding agonists and antagonists, was considered as a possible sensor. Given that R295$^{7.40}$ bears a permanent positive charge it makes sense that it might be involved in sensing changes in membrane potential and in relaying the information across the membrane for downstream signalling. Cryogenic electron microscopy (cryo-EM) studies of membrane-integral ion channels in an applied electric field suggest[2] that the investigation of voltage-dependent modulation of GPCR function is likely to become an important sub-discipline within the field[3].

**MD Simulations**

We performed molecular dynamics (MD) simulations of our cryo-EM structures of the TP in the presence and absence of the agonists U46619 and I-BOP. In addition, endogenous thromboxane, $TXA_2$ was docked to the TP and their corresponding complexes were simulated. Agonist complexes were simulated in the presence and absence of the $G_q$ heterotrimer. We also simulated structures of the TP with and without the antagonists, ramatroban and daltroban, embedded in a hydrated lipid bilayer. The goal was to compare the stability, dynamics, and interactions within the different complexes. The lipid composition used in simulations matched the natural glycerophospholipid, sphingolipid, and cholesterol composition of platelets. The root mean square deviation (RMSD) and fluctuation (RMSF) of the Cα atoms were analysed for the entire receptor and its transmembrane domain. The RMSD and RMSF were also calculated for the non-hydrogen atoms of the ligand in the receptor-ligand complexes. These analyses showed that the complexes were stable and experienced only minor fluctuations (Supplementary Table 2). A reliability and reproducibility checklist for our MD simulations is provided in Supplementary Table 3.

**Ligand interactions at the binding site**

By incorporating water molecules and molecular dynamics, we found evidence of additional polar interactions between I-BOP/U46619/$TXA_2$ and the TP compared with the static cryo-EM structures. Specifically, the agonist carboxyl group forms a hydrogen bond network with $H89^{2.65}$, $S181^{ECL2}$, and $R295^{7.40}$ facilitated by bridging waters (Supplementary Figs. 6 and 7). Interestingly, ligand binding is more stable when $H89^{2.65}$ is protonated (Supplementary Table 2). To evaluate the protonation status of $H89^{2.65}$, we estimated the $pK_a$ of $H89^{2.65}$ by calculating titration curves from constant pH simulations of ligand-bound and empty forms of TP. We found that the presence of the ligand shifts $pK_a$ to more basic values, resulting in the ligand-bound forms being fully protonated at physiological pH (pH 7.4; Supplementary Fig. 5).

Additionally, water-mediated interactions were observed between the bicyclic ring oxygen and $T298^{7.43}$ (Supplementary Figs. 6 and 7). The agonist hydroxyl group donated a hydrogen bond to the carbonyl oxygen of $Q301^{7.46}$ side chain (Supplementary Fig. 6), which formed early in, and remained stable throughout, the MD simulations (Supplementary Fig. 6b).

The antagonist carboxyl group also engages in hydrogen bonding with H89$^{2.65}$, S181$^{ECL2}$, and R295$^{7.40}$ (Supplementary Fig. 6). However, the sulfonyl group of the antagonists acts as a hydrogen bond acceptor interacting strongly with the Q301$^{7.46}$ amide instead of behaving as a hydrogen bond donor like the hydroxyl group of the agonists (Supplementary Fig. 6b). The antagonist's amide forms a strong hydrogen bond with T81$^{2.57}$ (Supplementary Fig. 6b).

Analysis of the average ligand-residue interaction energies revealed other key binding interactions for the agonists (Supplementary Fig. 14). In addition, hydrogen bond interactions occurred between the ligand and the backbone of A31$^{1.39}$ and F30$^{1.38}$ and the side chains of S27$^{1.35}$, P179$^{ECL2}$, and W182$^{ECL2}$ further stabilising the carboxyl group of the ligand. Strong van der Waals interactions were observed between the agonists and A31$^{1.39}$, L78$^{2.54}$, T81$^{2.57}$, V85$^{2.61}$, M112$^{3.32}$, W182$^{ECL2}$, L294$^{7.39}$, and T298$^{7.43}$ over the course of the MD simulations.

**Activation mechanism**

In the antagonist-bound receptors, our simulations agree with the crystal structures showing Q301$^{7.46}$ hydrogen bonding with W258$^{6.48}$ to maintain the inactive state (Supplementary Fig. 6b). Upon agonist binding, Q301$^{7.46}$ loses this bond and, instead, interacts with the agonist hydroxyl group (Supplementary Fig. 6b). This enables W258$^{6.48}$ to form a hydrogen bond with N300$^{7.45}$ (Supplementary Fig. 6), leading to TM7 rotation as seen in the simulations and cryo-EM structures (Supplementary Fig. 15). Thus, W258$^{6.48}$ adopts inactive or active conformations by interacting with Q301$^{7.46}$ or with N300$^{7.45}$, respectively (Supplementary Fig. 6).

We simulated D74$^{2.50}$ in the protonated state, as it is predicted to be protonated during activation of other GPCRs. This protonated D74$^{2.50}$ forms a hydrogen bond with D304$^{7.49}$ of the D$^{7.49}$P$^{7.50}$xxY$^{7.53}$ motif, bringing the Q301$^{7.46}$ backbone close to the amide side chain of N42$^{1.50}$ to form a hydrogen bond (Supplementary Fig. 6b). This has the effect of drawing TM7 closer to TM1, TM2, and TM3, stabilizing the hydrogen bond between G123$^{3.43}$ and Y308$^{7.53}$ of the D$^{7.49}$P$^{7.50}$xxY$^{7.53}$ motif indicative of activation (Supplementary Fig. 6b). Importantly, we do not observe this network involving D74$^{2.50}$ in antagonist-bound simulations, where TM7 remains dynamic (Supplementary Fig. 15).

The tighter clustering between TM1, TM2, TM3, and TM7 upon activation displaces internal water molecules towards TM4, TM5, and TM6 (Supplementary Fig. 6). This likely facilitates

the known outward movement of TM5 and TM6 during activation. The simulations show TM6 exhibits increased mobility and outward displacement with the agonist bound (Supplementary Fig. 15). Additionally, the R130$^{3.50}$ of the E$^{3.49}$R$^{3.50}$Y$^{3.51}$ motif shifts towards an active conformation, moving away from E129$^{3.49}$ especially when the $G_q$ heterotrimer is present (Supplementary Fig. 6b).

**Ligand binding**

Since the extracellular portion of the TP is occluded by ECL2, ECL3 and the N-terminus, we used random accelerated MD (RAMD) to explore dissociation pathways for agonists and antagonists. In RAMD, a random force is applied to the ligand centre of mass in various directions to generate a dissociation trajectory. The bulkier and more rigid antagonists, ramatroban and daltroban, primarily exited through the gap between the extra-cytoplasmic halves of TM1 and TM7 towards the lipid bilayer (96% and 84% of the trajectories) (Supplementary Fig. 10). In contrast, the more flexible agonists, U46619 and I-BOP, showed two main bilayer escape routes, namely the TM1/TM7 gap (40% and 32%) and the TM1/TM2 gap (50% and 46%). With much reduced frequency, the agonists also exited extracellularly between TM1, TM2, TM3, and ECL2 (6% and 13%), and to the bilayer through the TM2/TM3 gap (4% and 9%) (Supplementary Fig. 10). The high flexibility of TM1 seen in conventional simulations explains its featured role.

## Supplementary Figures

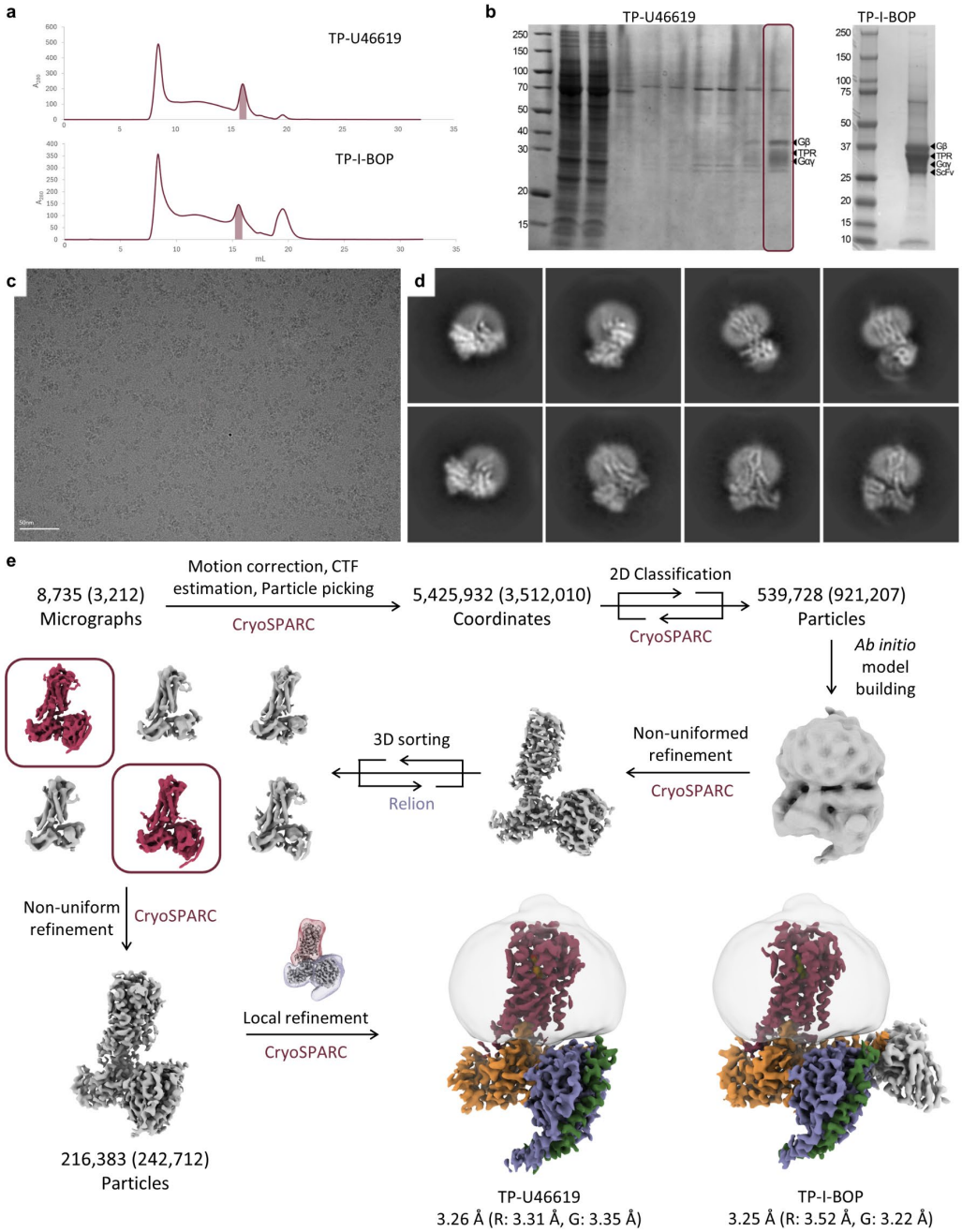


**Supplementary Fig. 1 | Protein purification and cryo-EM flowchart. a** Size exclusion chromatography (SEC) profile of the TP complex purified with the agonists U46619 (top) and I-BOP (bottom). Fractions corresponding to the monomer peak (dark red) were combined and used for the cryo-EM studies. **b** Coomassie-stained SDS-PAGE indicating the presence of the receptor and the $G_q$ heterotrimer in the samples used for the structural studies. Data for TP-U46619 is presented to the left. The relevant lane containing the SEC fraction used for the EM studies is boxed with a red line. The TP-I-BOP complex (presented to the right) was prepared in the presence of scFv16. The band corresponding to scFv16 is labelled (ScFv). **c** Representative cryo-EM micrograph of the TP-I-BOP complex. **d** Representative reference-free 2D class averages. The diameter of the circular mask is 20 nm. **e** Processing flowchart of the cryo-EM data, including particle selection, 2D and 3D classifications, particle sorting, masking, and final map reconstruction. Data processing was done using a combination of CryoSPARC 4.2.1[4,5] and Relion 4.0[6,7]. The software used for each step is indicated in the flowchart.

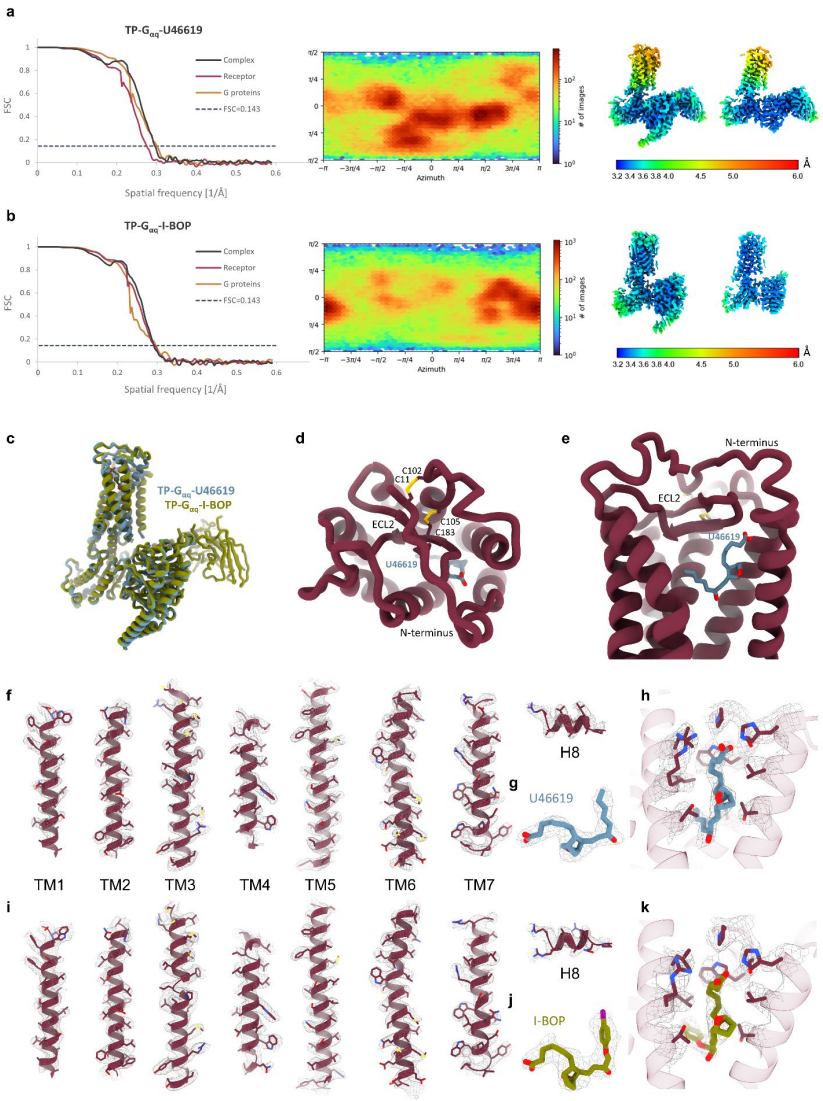


**Supplementary Fig. 2 | EM map, model quality and structural features of the activated TP. a-b** *Left:* Gold standard Fourier shell correlation (FSC) curves of half maps that were individually calculated for each reconstitution. The map calculated for the entire complex is in black. The maps calculated for the receptor alone and for the $G_q$ heterotrimer alone are shown in red and gold, respectively. Resolutions for the TP-U46619 complex, receptor alone, and $G_q$ heterotrimer alone are 3.26 Å, 3.31 Å and 3.35 Å, respectively (**a**). Resolutions for the TP-I-BOP complex, receptor alone, and $G_q$ heterotrimer alone are 3.25 Å, 3.52 Å and 3.22 Å, respectively (**b**). Resolutions were calculated at 0.143 FSC. *Middle:* Angular distribution of particles for the final 3D reconstructions. *Right:* EM density map coloured by local resolution (calculated by Phenix). Colour represents the resolution in Å units. Side view (left) and cut through (right) of the map are shown. The map contour level is 0.3 and 0.25 for TP-U46619 (**a**) and TP-I-BOP (**b**), respectively. **c** Superposition of the two active structures with TP-U46619 (blue) and TP-I-BOP (green) indicating that the models are very similar with an all-atom RMSD value of 0.5 Å. **d-e** Two unique disulfide bonds are formed between $C11^{N\text{-term}}$ and $C102^{3.22}$, and between $C105^{3.25}$ and $C183^{ECL2}$, that create a rigid 2-layer lid in TP-U46619 that limits access of ligands to the orthosteric pocket from the extracellular milieu. Top (**d**) and side (**e**) views show disulfide positions and highlights the lid composed of ECL2 and the N-terminus. **f-h** Snapshots of model in density of the U46619-bound structure for TM1-7 and H8 (**f**), the ligand U46619 (**g**), and the binding pocket surface (**h**). The map contour level is 0.2 for the TMs and ligand, and 0.3 for the pocket representation. **i-k** Snapshots of model in density of the I-BOP bound structure for TM1-7 and H8 (**i**), I-BOP (**j**) and the binding pocket surface (**k**). The map contour level is 0.15 for the TMs and ligand, and 0.2 for the pocket representation.

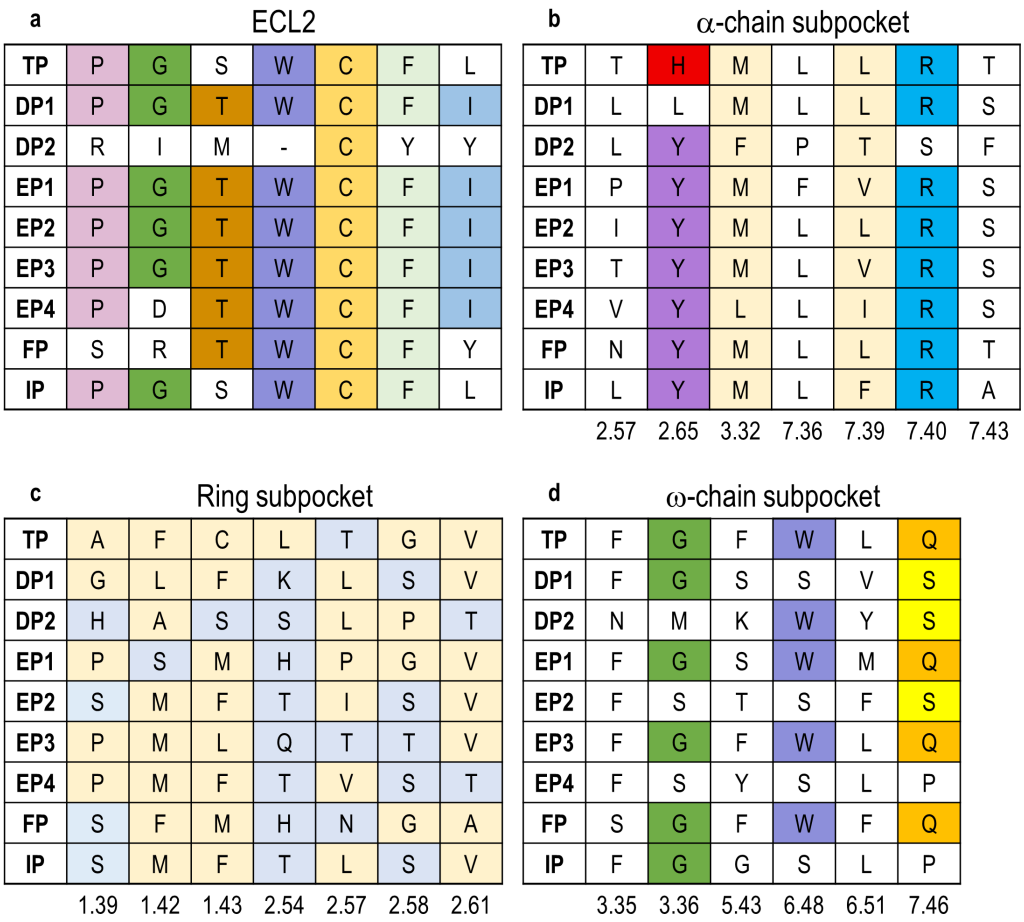


**Supplementary Fig. 3 | Sequence alignment of the TP with other prostanoid receptors. a** The ECL2 of prostanoid receptors consists of a highly conserved PGTWCFI motif (consensus sequence highlighted in different colours) that forms the ceiling of the binding pocket. **b-d** Selected residues forming the α-chain (**b**), ring (**c**), and ω-chain (**d**) subpockets of the TP and their alignment with other prostanoid receptors. The Ballesteros-Weinstein residue numbers are shown below each column. In (**a**), the conserved $Y^{2.65}$ and $R^{7.40}$ residues that interact with the carboxylic acid group of endogenous prostanoid ligands are coloured purple and blue, respectively. The TP and DP1 are exceptions. The TP has a histidine (red) at position 2.65. Residues at positions 3.32 and 7.39 (cream) are all apolar and similar in size, playing a role in maintaining the correct geometry of the ligands. Polar and apolar residues in (**c**) are coloured light blue and cream, respectively, showing that the ring subpocket of TP is more apolar than the ring subpockets of other prostanoid GPCRs. $W^{6.48}$ is coloured navy in (**d**). The residue at position 3.36 often interacts with $W^{6.48}$ in other class A GPCRs, but the $G^{3.36}$ (green) in most prostanoid receptors is unable to do so. Polar Q and S residues (orange and yellow, respectively) are found at position 7.46. In the TP, a conservative mutation of $Q^{7.46}$ to $S^{7.46}$ did not abolish receptor activity.

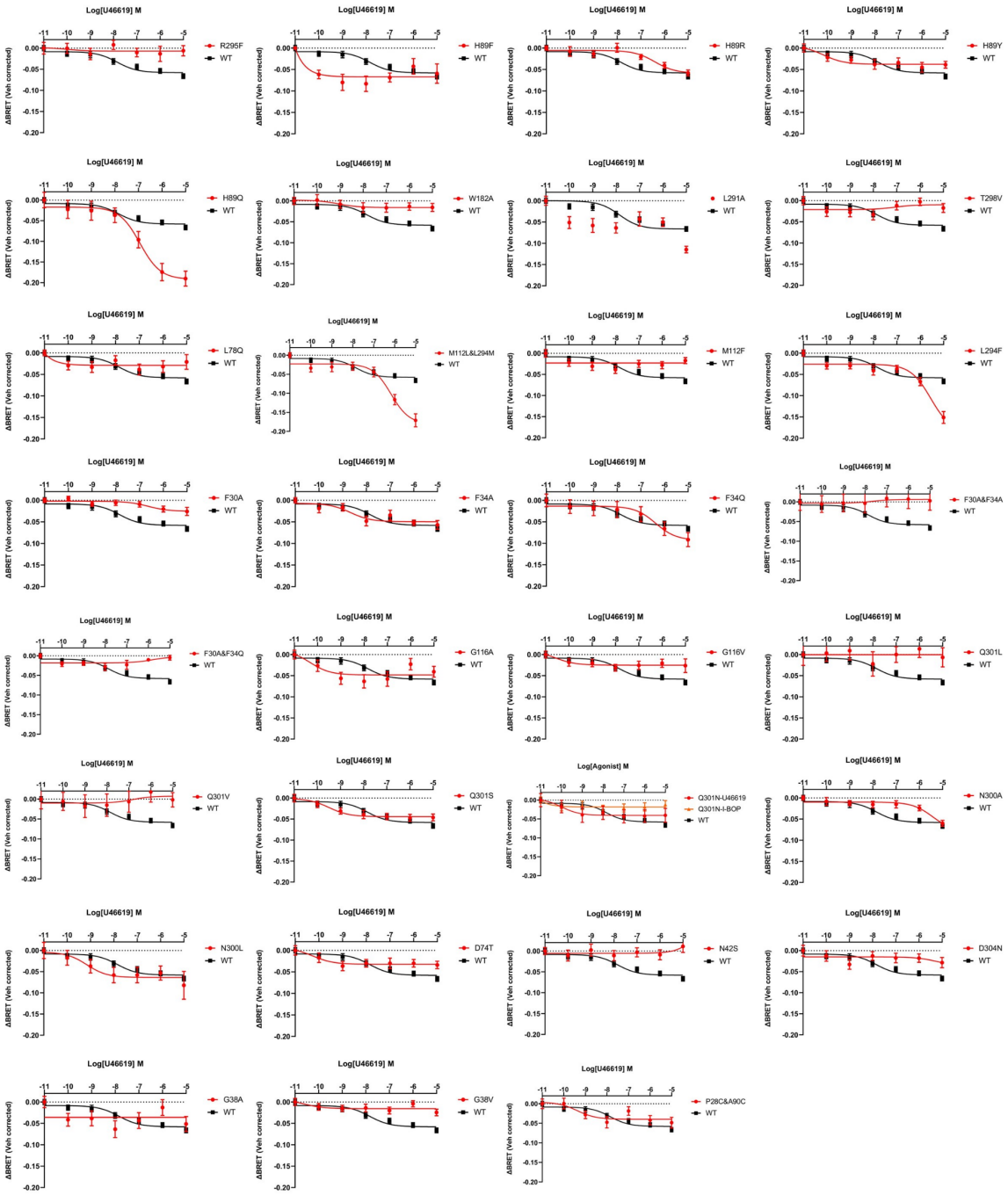


**Supplementary Fig. 4 | BRET signalling assays of TP mutants.** Dose-response curves of TP mutants following stimulation with U46619 and/or I-BOP (final concentration range of $10^{-11}$ – $10^{-5}$ M). Data are presented as the mean ± SEM of 3 independent experiments (n=3) performed in technical triplicate.

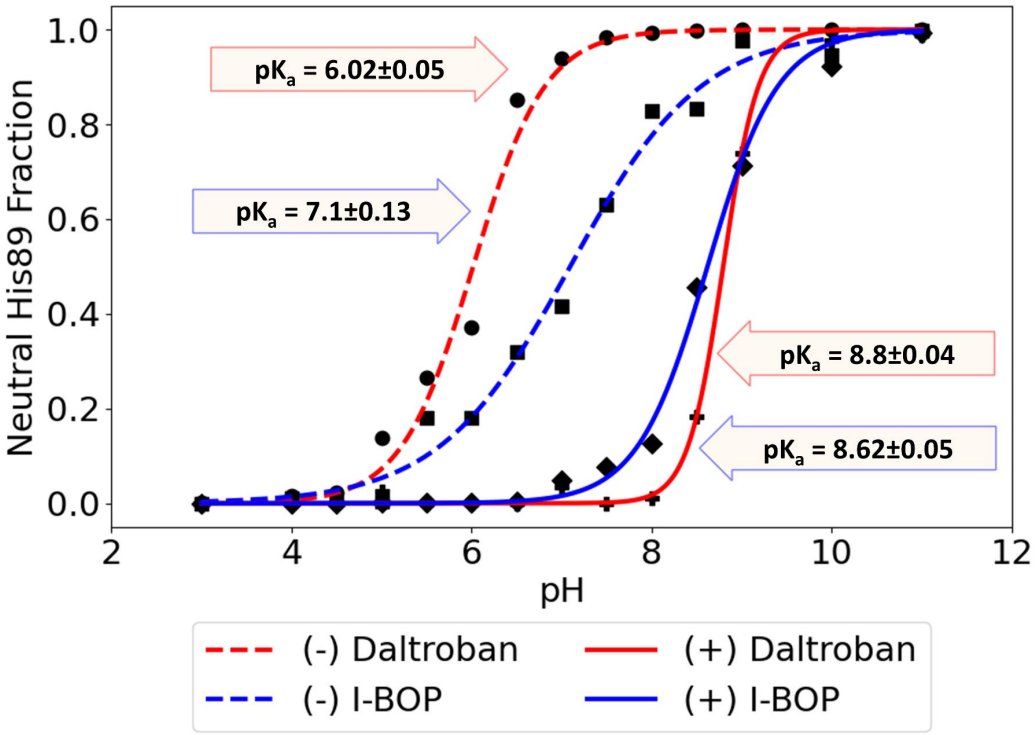


**Supplementary Fig. 5 | pH titration curves and estimated pK$_a$ values for H89$^{2.65}$ computed from constant pH simulations of the TP with or without bound antagonist (daltroban) or agonist (I-BOP).** Ligand binding produces a shift in pK$_a$ to more basic values making the imidazole of H89$^{2.65}$ in the ligand-bound receptor fully protonated (positively charged) at physiological pH.

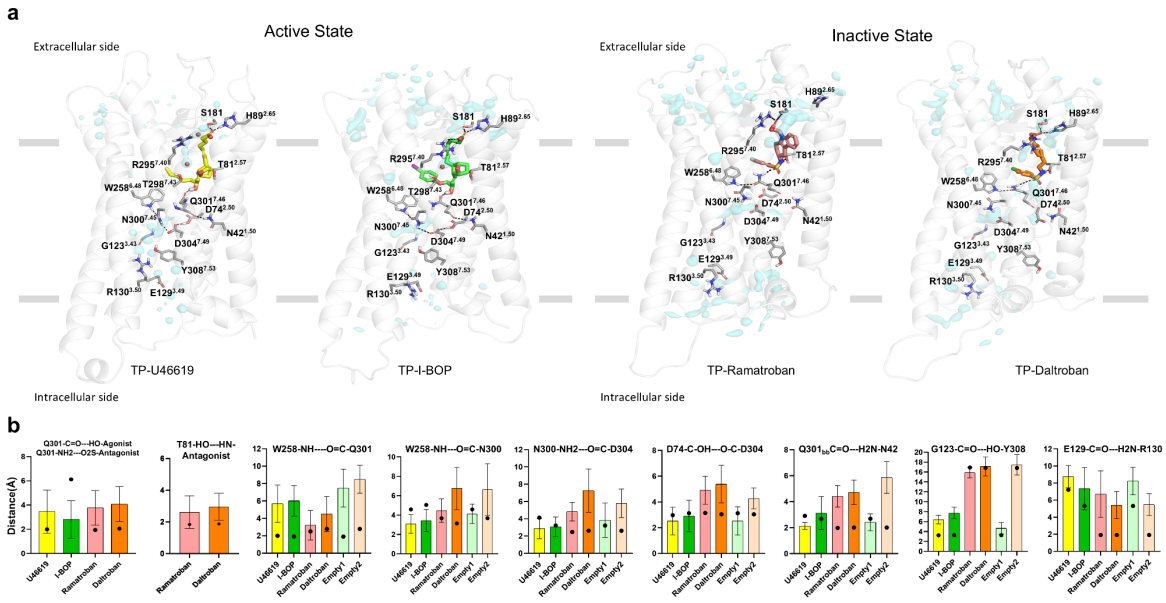


**Supplementary Fig. 6 | MD simulations reveal the distinct hydrogen bond networks that agonists and antagonists form with the TP. a** Representative simulation snapshots of the agonists, U46619 (yellow) and I-BOP (green), and antagonists, ramatroban (pink) and daltroban (orange), bound to the TP. Key residues involved in receptor-ligand interactions and receptor activation are shown. Black dashes indicate hydrogen bonds, cyan surfaces show internal water molecules. **b** Dynamics of key hydrogen bonding interactions in agonist- and antagonist-bound TP complexes. Mean distances between atoms involved in hydrogen bonding during MD simulations (≥1 μs, n=3) are shown. Simulations were initiated from U46619- or I-BOP-bound (agonists, yellow/green), ramtroban- or daltroban-bound (antagonists, pink/orange) structures, and empty receptors from U46619- and daltroban-bound complexes (light green/orange). Black dots represent distances in cryo-EM structures. Key findings include: stable hydrogen bonds (donor-acceptor distance <3.5 Å) between $Q301^{7.46}$(C=O)-agonist(OH) and $Q301^{7.46}$($NH_2$)-antagonist($SO_2$); stable $T81^{2.57}$-antagonist hydrogen bond; $W258^{6.48}$ hydrogen bond switch between $Q301^{7.46}$ (antagonist-bound) and $N300^{7.45}$ (agonist-bound); agonist-specific hydrogen bonds ($N300^{7.45}$-$D304^{7.49}$, $D74^{2.50}$-$D304^{7.49}$, $Q301^{7.46}$-$N42^{1.50}$, $G123^{3.43}$-$Y308^{7.53}$); and $E129^{3.49}$-$R130^{3.50}$ ionic lock of the $E^{3.49}R^{3.50}Y^{3.51}$ motif breaking (donor-acceptor distance >5 Å) in agonist-bound but not in antagonist-bound complexes. These interactions highlight distinct conformational changes associated with agonist and antagonist binding, providing insights into TP activation mechanisms.

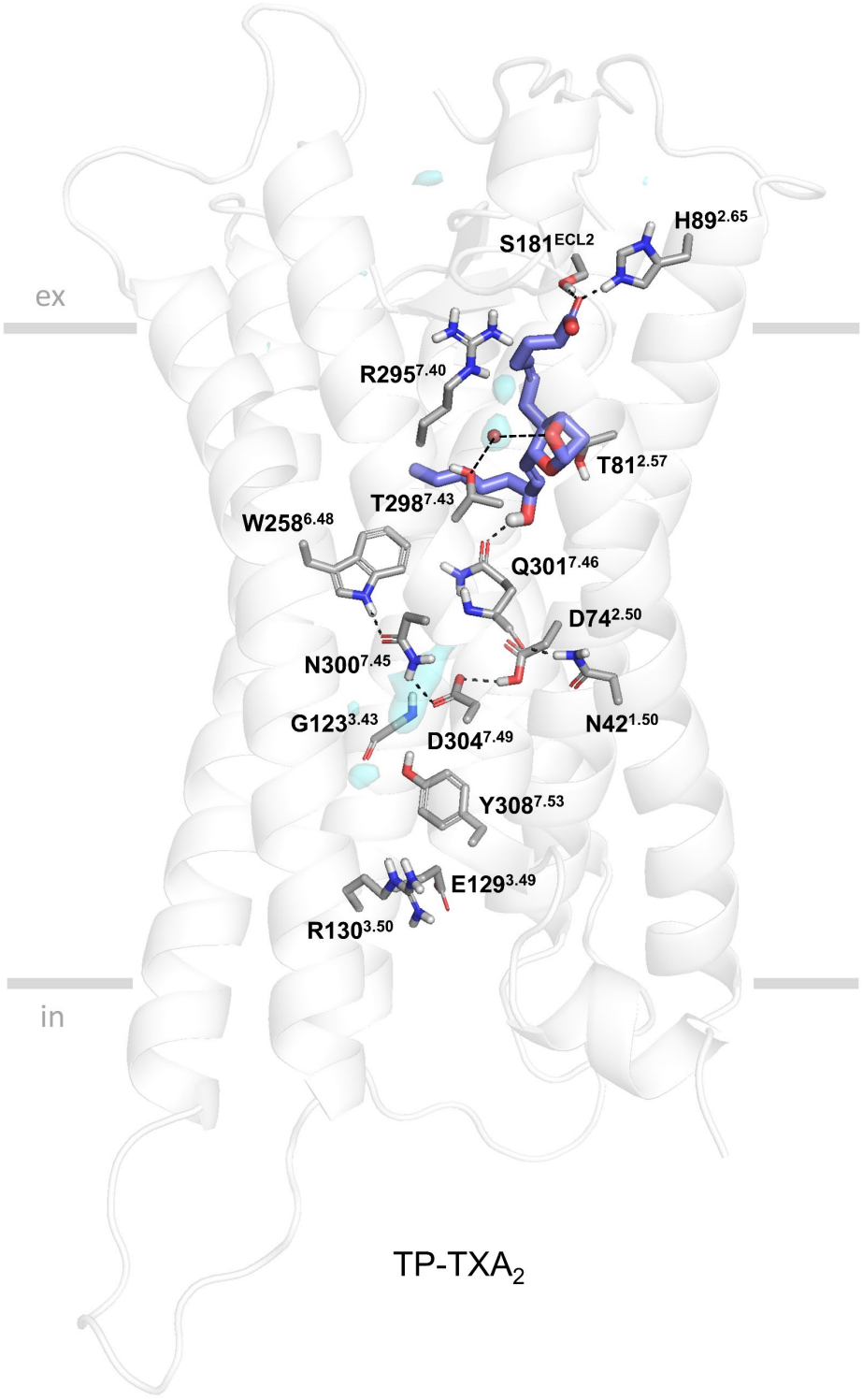


**Supplementary Fig. 7 | Binding mode of $TXA_2$ and the TP from MD simulations.** Representative snapshot of the TP bound to its endogenous ligand $TXA_2$ (violet) from MD simulations. Residues involved in a hydrogen bond network with the ligands and the activation mechanism are shown in stick representation. Hydrogen bonds are shown as black-dashed lines. Water clusters observed in the MD simulations are shown in cyan surface representation. A water molecule, which facilitates interaction between the bicyclic ring oxygen of the agonists and T298$^{7.43}$, is depicted as a red ball representing the oxygen atom.

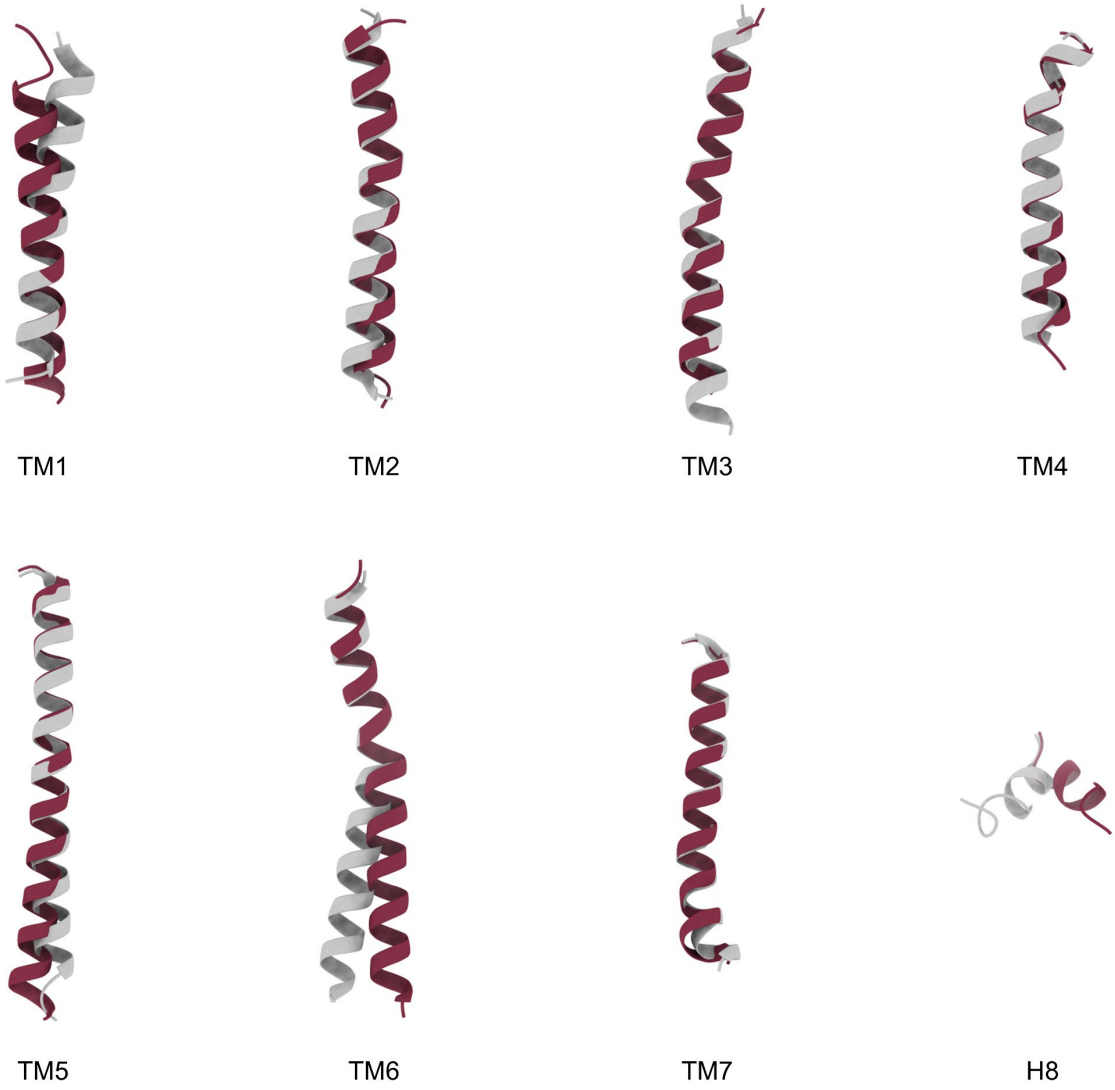


**Supplementary Fig. 8 | Comparison of active and inactive states of the TP by helix.** Structural alignment of transmembrane and C-terminal helix positions in the active state receptor bound to U46619 (red) and inactive structure bound to ramatroban (PDB ID 6IIU, grey), showing pronounced conformational changes at the extracellular (upper) face of TM1, and at the intracellular (lower) segment of TM6 and H8.

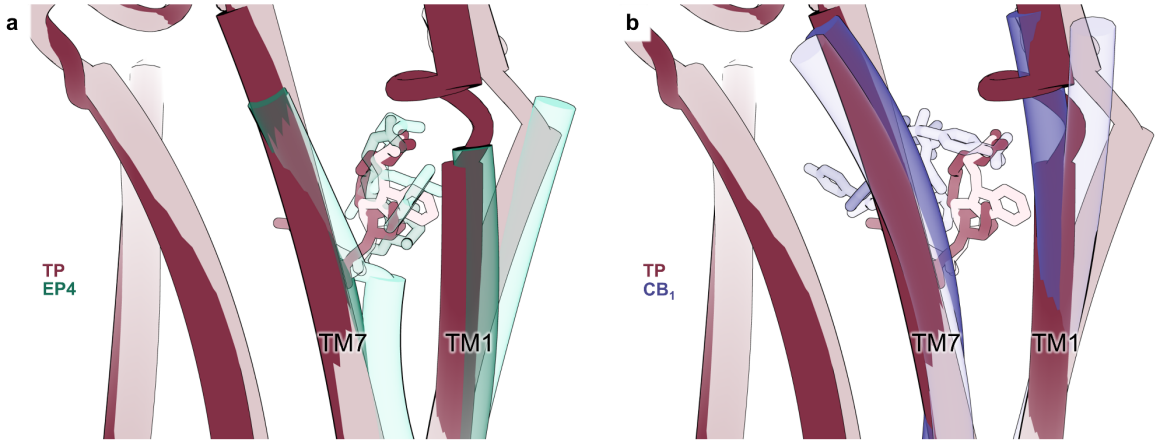


**Supplementary Fig. 9 | Relative movement of TM1 and TM7 in the TP and other receptors upon activation. a** Comparing the TP (red, active – U46619; pink, inactive – ramatroban) with EP4 (active – $PGE_2$, dark green – PDB 7D7M; inactive – ONO-AE3-208, light green – PDB 5YMY) indicating that the conformational change of TM1 associated with receptor activation is larger in the TP. **b** Comparing the TP (red, active – U46619; pink, inactive – ramatroban) with the cannabinoid receptor type 1 ($CB_1$) (purple, active – MDMB-fubinaca - PDB 6N4B; light purple, inactive – taranabant - PDB 5U09) showing a significantly larger opening of the gap in the TP. $CB_1$ is an example of a non-prostanoid receptor.

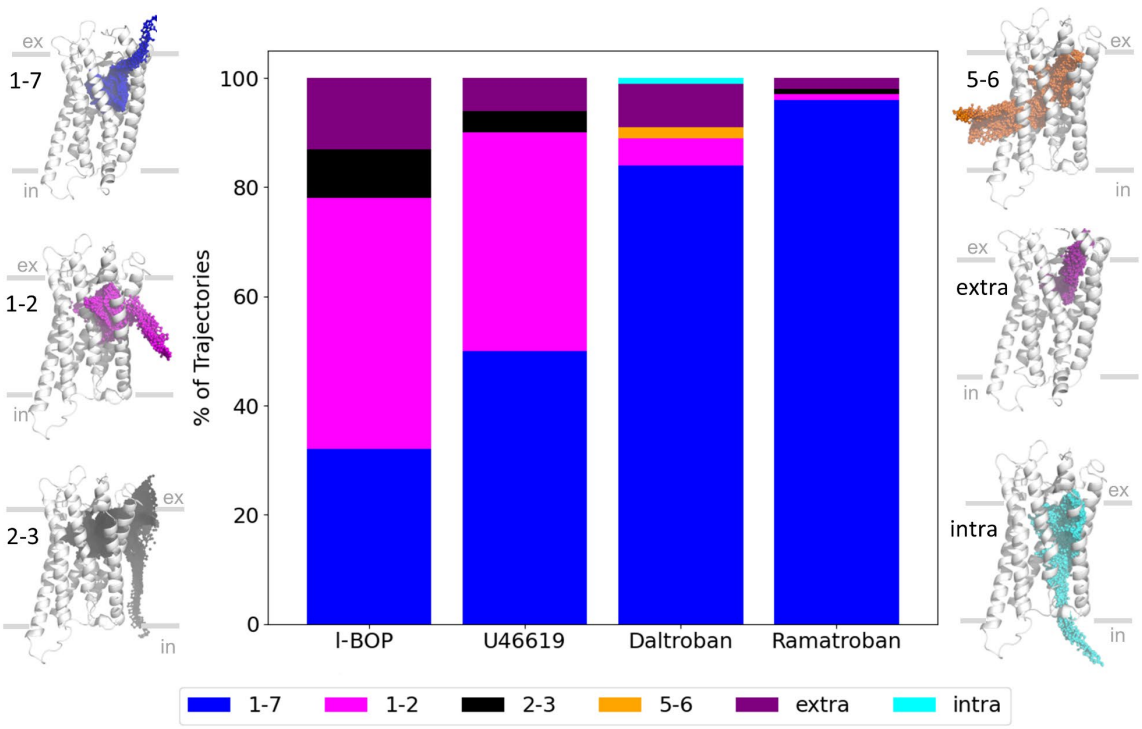


**Supplementary Fig. 10 | Routes by which agonists and antagonists dissociate from the TP as determined by RAMD simulations.** The bar plot shows the percentage of each ligand exiting route observed in RAMD simulations of the agonist and antagonist complexes. Dissociation routes lie between TM1 and TM7 (1-7, blue), between TM1 and TM2 (1-2, magenta), between TM2 and TM3 (2-3, black), between TM5 and TM6 (5-6, orange), towards the extracellular milieu (extra, purple), and towards the cytoplasm (intra, cyan). Percentage values are reported in the Supplementary Discussion.

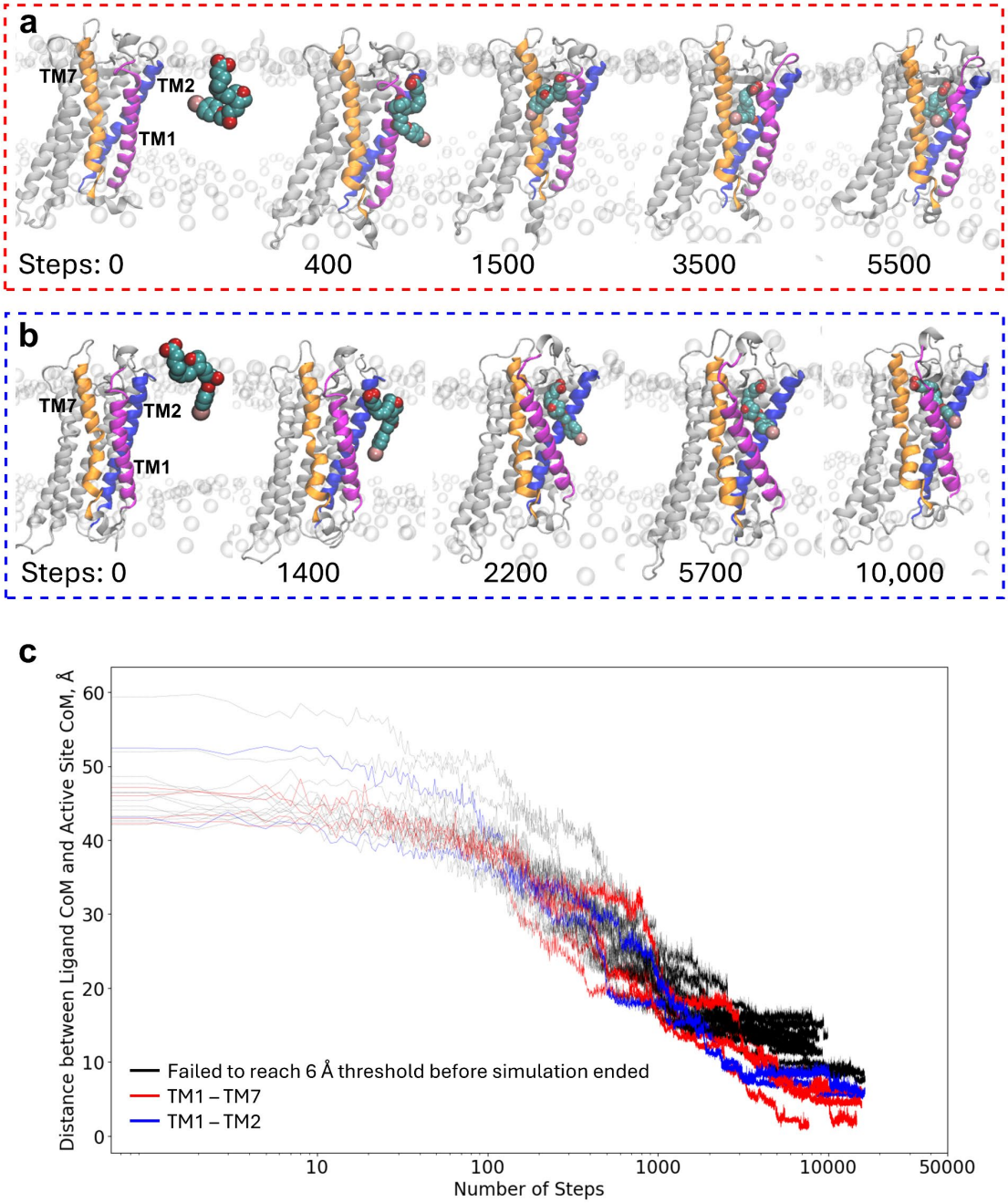


**Supplementary Fig. 11 | I-BOP entry pathways through TM1-TM7 and TM1-TM2 gaps in the TP.** **a-b** suMD simulation snapshots showing I-BOP (teal carbon spheres) binding to the TP through two distinct membrane entry pathways: **(a)** via the TM1-TM7 gap and **(b)** via the TM1-TM2 gap. Transmembrane helices are colored as follows: TM1 (purple), TM2 (blue), and TM7 (orange). Numbers indicate simulation steps progressing from ligand approach to binding site entry. **c** Distance evolution between centers of mass (CoM) of I-BOP and the TP binding site across 20 independent suMD simulations. The x-axis represents the cumulative number of 150,000-step simulation cycles (both successful and unsuccessful attempts) performed for each system. The y-axis shows the distance between ligand and binding site CoMs. Six simulations successfully reached the 6 Å threshold: four trajectories (red) entered via the TM1-TM7 gap, with two of these achieving close approach (≤2 Å), while two trajectories (blue) entered via the TM1-TM2 gap. Simulations that did not reach 6 Å by the time the simulation ended are shown in black.

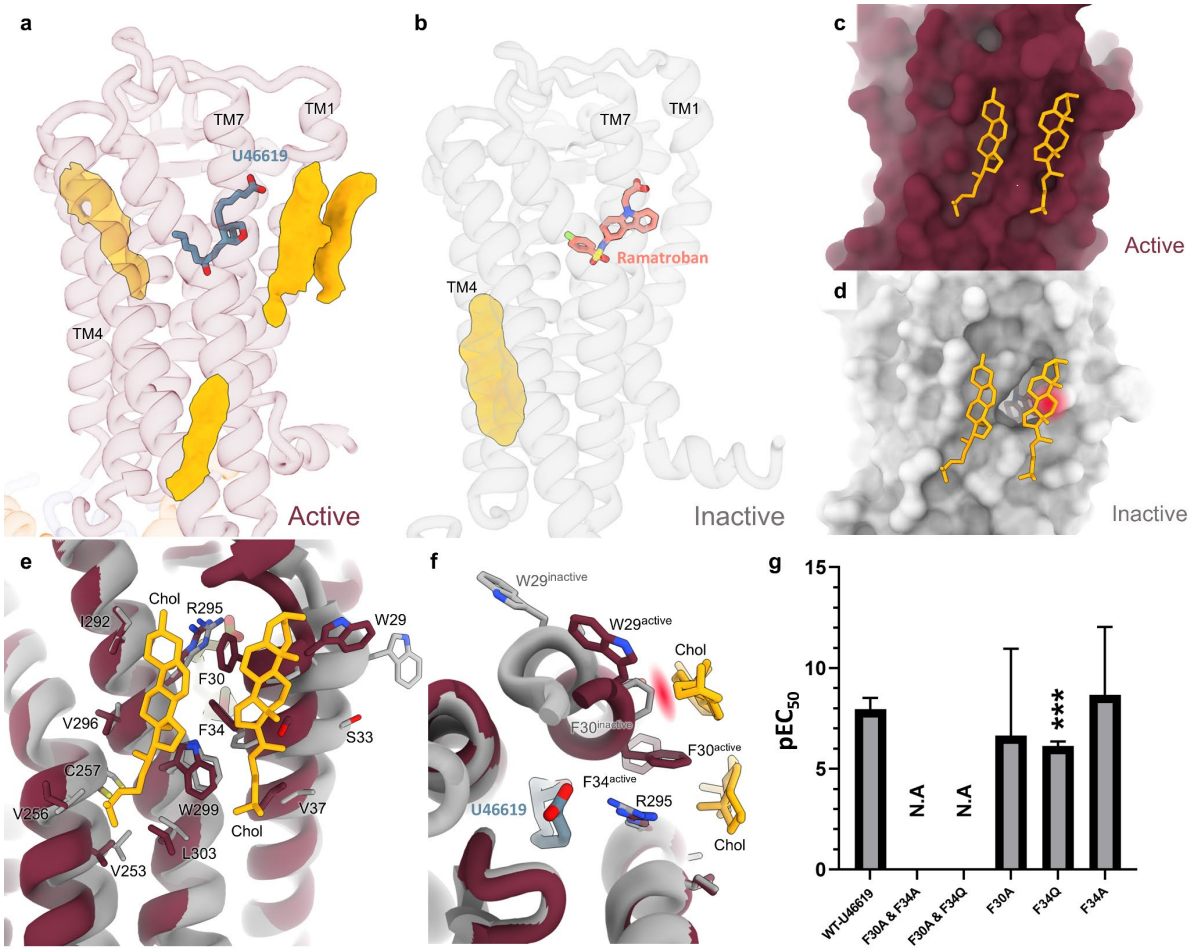


**Supplementary Fig. 12 | Cholesterol binding at the TM1/7 cavity in the TP. a** Four cholesterol* molecules were captured within the EM density. Three cholesterols are located toward the extracellular half of the receptor in close proximity to TM1, TM6, and TM7, while one is toward the intracellular half of the receptor next to TM5. **b** Cholesterol was also found in the inactive crystal structure of TP (PDB 6IIU). In contrast to the active state, only one cholesterol molecule is bound in the inactive structure. It is located toward the intracellular half of the receptor in close proximilty to TM4. **c** Surface representation of TP in the active state (U46619-bound) with cholesterol bound next to the hydrophobic cavity created by the gate at the TM1/TM7 interface. **d** Superposition of cholesterol binding pose in the active state (U46619-bound), with the inactive receptor structure (grey, PDB 6IIU) indicating that the cavity for cholesterol binding is absent in the inactive receptor state. In addition, the conformational change in $F30^{1.38}$ in the inactive state clashed with the cholesterol position in the active state. Clash is indicated in red. **e** Residues that compose the cholesterol gate binding site in the active TP (red) superposed with their couterparts in the inactive TP (grey, PDB 6IIU). **f** Top view of the superposition presented in (**e**), highlighting the clash (red) between $F30^{1.38}$ of the inactive state and one of the bound cholesterol molecules in the active state. **g** $EC_{50}$ values in response to mutations in the residues composing the TP gap/cholesterol binding cavity. $EC_{50}$ values are not available for mutants marked with N.A as their data did not fit dose-response curves. Data are presented as mean ± SEM from three independent experiments. *** indicates $P < 0.001$. Statistical significance was determined by one-way ANOVA followed by Dunnett's post-hoc tests, comparing the mutants treated with U46619 to the corresponding WT treated with U46619.

*Note that the TP was purified in the presence of cholesteryl hemisuccinate (CHS) that can hydrolyze to cholesterol. We thus modeled cholesterol, albeit we cannot exclude the possibility that some of the modeled cholesterol moieties could be CHS.

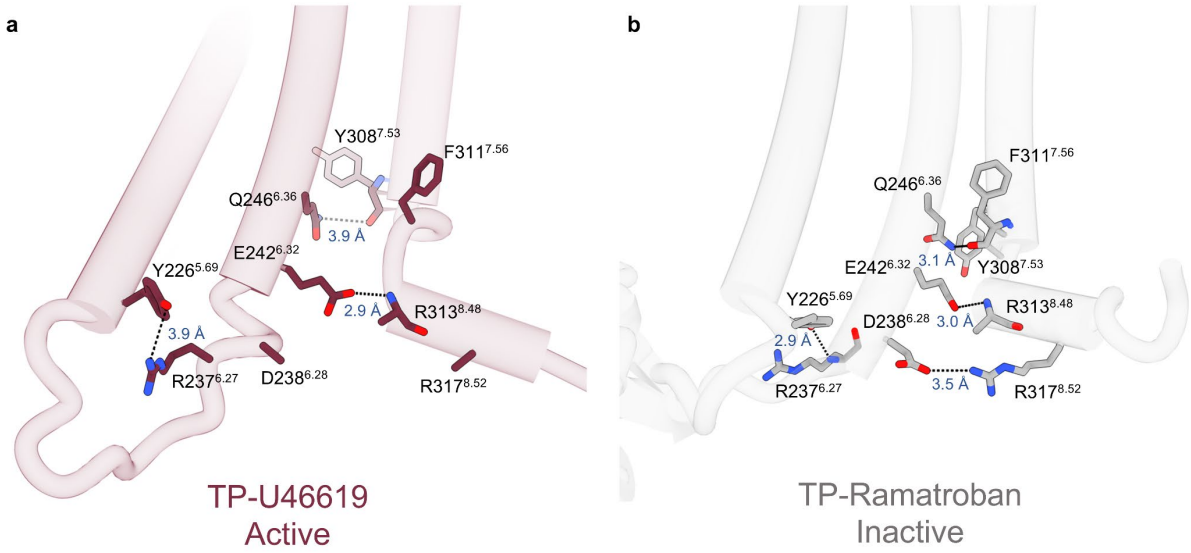


**Supplementary Fig. 13 | Conformational differences between the intracellular face of the active and inactive states of the TP. a** Hydrogen bond network among residues in the U46619-bound active TP. **b** Hydrogen bond network among residues in the inactive TP (ramatroban, PDB 6IIU). Hydrogen bonds are marked with a dashed line with distances in Å.

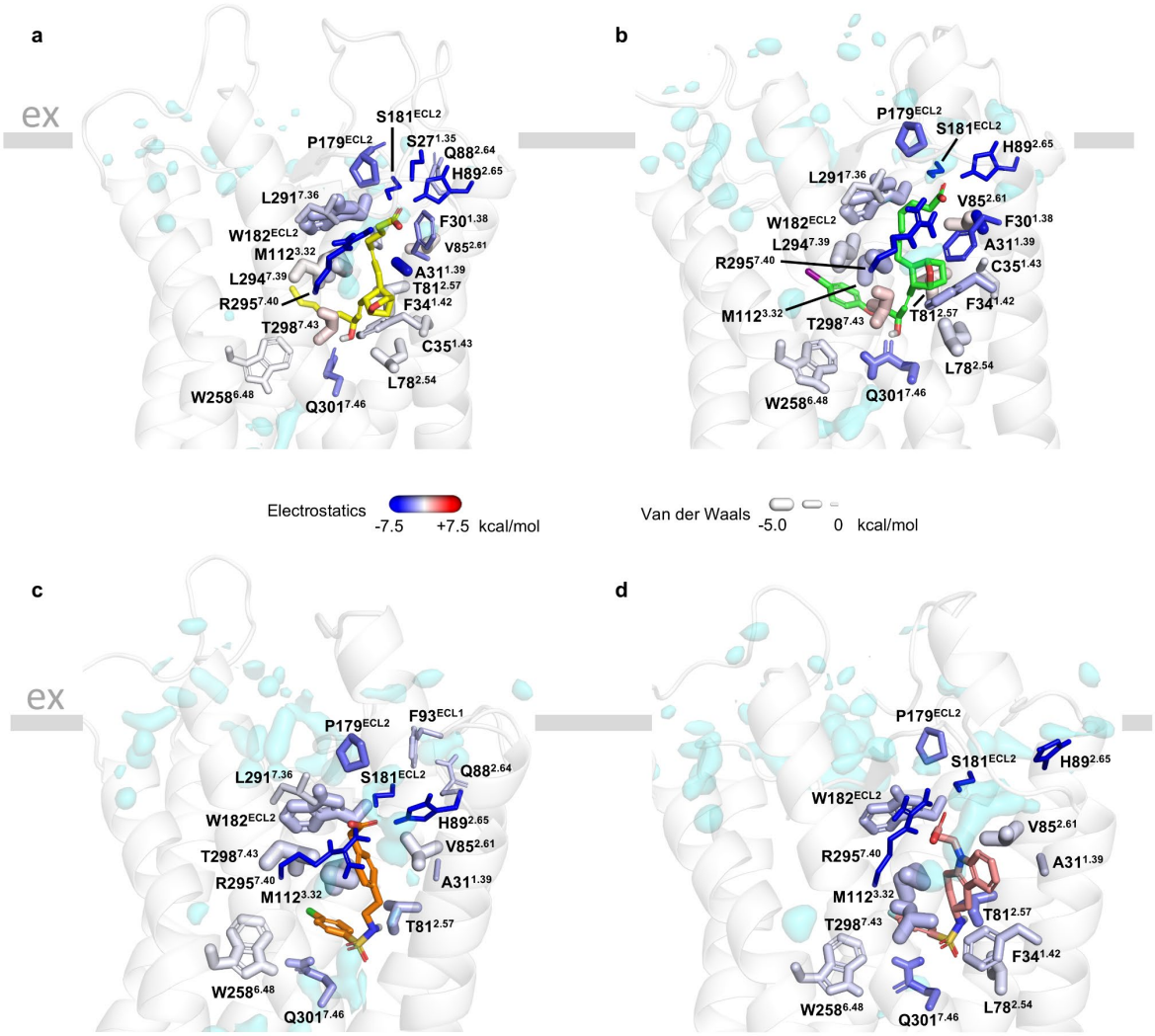


**Supplementary Fig. 14 | Ligand-residue interactions in the TP probed by MD simulations. a** TP-U46619. **b** TP-I-BOP. **c** TP-Daltroban. **d** TP-Ramatroban. A representative frame is shown with key residues forming contacts with U46619 (yellow), I-BOP (green), daltroban (orange), and ramatroban (pink). The size and colour of the residues correspond to the average strength of van der Waals and electrostatic interactions with the ligands, respectively (key as inset). Water clusters observed in the MD simulations are shown in cyan surface representation.

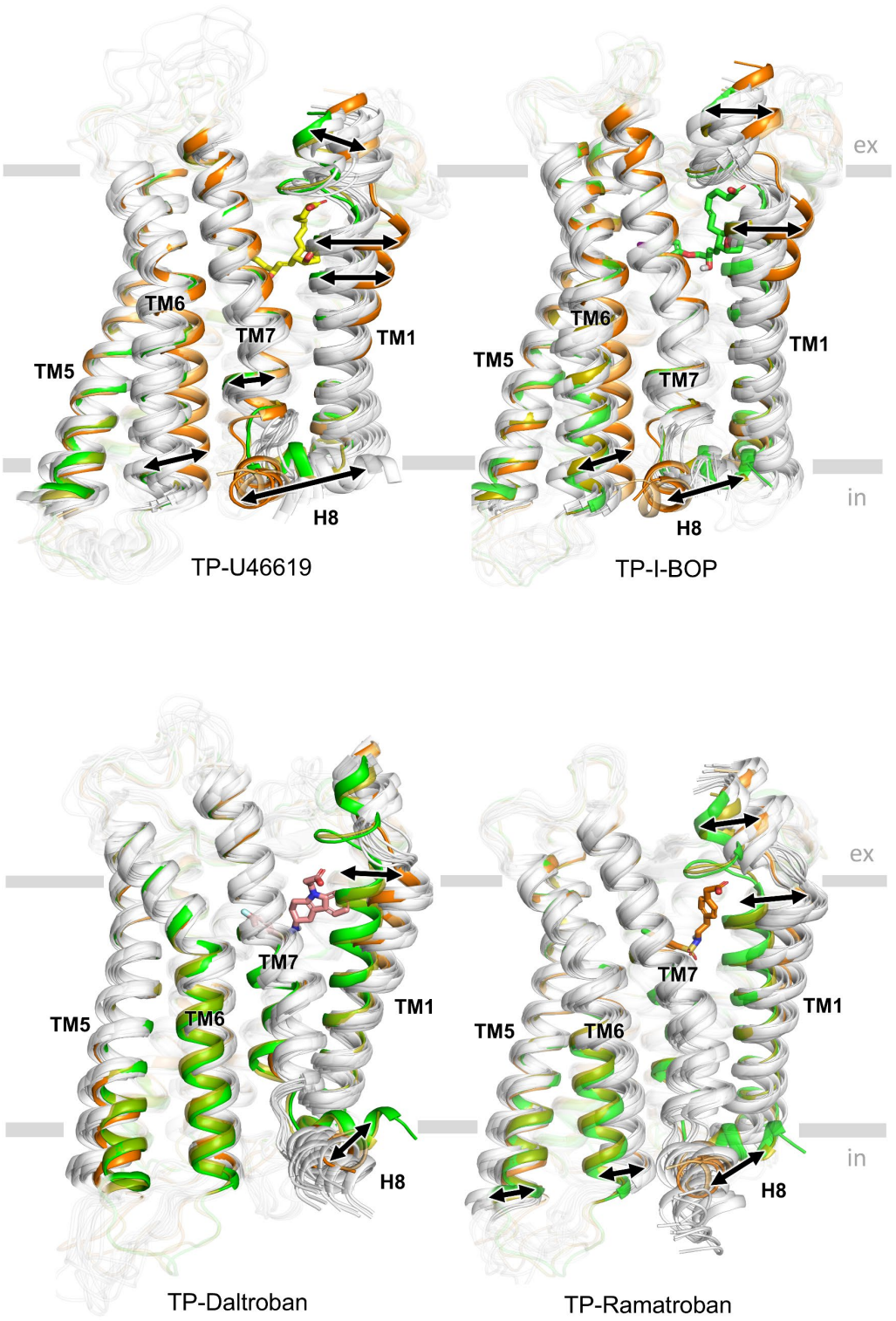


**Supplementary Fig. 15 | Agonists and antagonists differentially affect transmembrane helix mobility in the TP.** Overlays compare representative conformations from MD simulations of I-BOP-, U46619-, daltroban-, and ramatroban-bound receptor complexes (white) with corresponding experimental structures (light and normal green, light and normal orange, respectively). Arrows indicate the most notable fluctuations of TM1, TM5, TM6, TM7, and H8 between an active to inactive state during the simulations.

## Supplementary Tables

**Supplementary Table 1. Cryo-EM data collection, refinement, and validation statistics.**

| | TP-U46619 (EMDB-51324) (PDB 9GG5) | TP-I-BOP (EMDB-51324) (PDB 9GGG) |
|---|---|---|
| **Data collection and processing** | | |
| Magnification | 105,000 | 105,000 |
| Voltage (kV) | 300 | 300 |
| Electron exposure (e–/Å$^2$) | 38.4 | 38.4 |
| Defocus range (μm) | -0.8-(-2.0) | -0.8-(-2.0) |
| Pixel size (Å) | 0.826 | 0.826 |
| Symmetry imposed | C1 | C1 |
| Initial particle images (no.) | 5,425,932 | 3,512,010 |
| Final particle images (no.) | 216,383 | 242,712 |
| Map resolution (Å) | 3.26 (3.31,3.35) | 3.25 (3.52,3.22) |
| FSC threshold | 0.143 | 0.143 |
| Map resolution range (Å) | 3.26-12.59 | 3.25-12.74 |
| | | |
| **Refinement** | | |
| Initial model used (PDB code) | 6IIU | 6IIU |
| Model resolution (Å) | 3.6 | 3.6 |
| FSC threshold | 0.5 | 0.5 |
| Model resolution range (Å) | 3.26-12.59 | 3.25-12.74 |
| Map sharpening *B* factor (Å$^2$) | 121 (111.7,136.6) | 123.9(135.0,125.2) |
| Model composition | | |
| Non-hydrogen atoms | 6,938 | 8,656 |
| Protein residues | 929 | 1159 |
| Ligands | 5 | 5 |
| *B* factors (Å$^2$) | | |
| Protein | 92.04 | 181.81 |
| Ligand | 71.03 | 122.66 |
| R.m.s. deviations | | |
| Bond lengths (Å) | 0.002 | 0.002 |
| Bond angles (°) | 0.423 | 0.420 |
| Validation | | |
| MolProbity score | 1.15 (99$^{th}$ percentile) | 1.25 (99$^{th}$ percentile) |
| Clashscore | 1.69 (99$^{th}$ percentile) | 1.83 (99$^{th}$ percentile) |
| Poor rotamers (%) | 0 | 0 |
| Ramachandran plot | | |
| Favored (%) | 96.51 | 95.63 |
| Allowed (%) | 3.38 | 4.37 |
| Disallowed (%) | 0.11 | 0 |

*Numbers in parentheses are of the locally refined receptor and $G_q$ heterotrimer, respectively.

**Supplementary Table 2. The average RMSD and RMSF of the receptor systems.** RMSD and RMSF values were calculated for the Cα atoms of the entire receptor, the 7-transmembrane helical bundle (7TM) Cα atoms, and the ligand (non-hydrogen atoms). The calculations involved three 1 μs MD simulations for each receptor system. RMSD values were first averaged within each replica and combined between three replicas to yield the mean and standard deviation. RMSF values are also given as mean ± standard deviation between three different replicates.

| Receptor Systems* | RMSD, Å | | | RMSF, Å | | |
|---|---|---|---|---|---|---|
| | Cα | 7TM-Cα | Ligand | Cα | 7TM-Cα | Ligand |
| $TP_{U46619}$ | 3.1 ± 0.2 | 1.8 ± 0.1 | 1.8 ± 0.1 | 1.2 ± 0.0 | 0.8 ± 0.0 | 1.0 ± 0.1 |
| $TP_{empty_U46619}$ | 2.8 ± 0.2 | 1.6 ± 0.1 | | 1.3 ± 0.0 | 0.8 ± 0.1 | |
| $TP_{U46619_H89_unprot}$ | 3.2 ± 0.3 | 2.1 ± 0.2 | 1.9 ± 0.5 | 1.4 ± 0.0 | 1.0 ± 0.0 | 1.4 ± 0.0 |
| $TP_{I\text{-}BOP}$ | 2.6 ± 0.4 | 1.7 ± 0.3 | 2.0 ± 0.3 | 1.2 ± 0.1 | 0.9 ± 0.1 | 1.1 ± 0.1 |
| $TP_{empty_I\text{-}BOP}$ | 2.7 ± 0.2 | 1.7 ± 0.1 | | 1.1 ± 0.1 | 0.8 ± 0.1 | |
| $TP_{Ramatroban}$ | 2.6 ± 0.3 | 1.7 ± 0.3 | 1.6 ± 0.3 | 1.1 ± 0.1 | 0.8 ± 0.1 | 1.1 ± 0.2 |
| $TP_{empty_Ramatroban}$ | 2.7 ± 0.2 | 1.9 ± 0.2 | | 1.2 ± 0.1 | 0.9 ± 0.1 | |
| $TP_{Daltroban}$ | 2.7 ± 0.3 | 1.7 ± 0.1 | 2.0 ± 0.1 | 1.1 ± 0.2 | 0.8 ± 0.1 | 1.1 ± 0.0 |
| $TP_{empty_Daltroban}$ | 2.6 ± 0.1 | 1.6 ± 0.2 | | 1.1 ± 0.1 | 0.8 ± 0.1 | |

*Receptor systems include the TP-U46619 complex ($TP_{U46619}$), TP-I-BOP complex ($TP_{I\text{-}BOP}$), TP-Ramatroban complex ($TP_{Ramatroban}$), TP-Daltroban complex ($TP_{Daltroban}$), and the TP-U46619, TP-I-BOP, TP-Ramatroban, and TP-Daltroban complexes from which the ligand has been removed ($TP_{empty_U46619}$, $TP_{empty_I\text{-}BOP}$, $TP_{empty_Ramatroban}$, and $TP_{empty_Daltroban}$).

**Supplementary Table 3. MD simulations reliability and reproducibility checklist.**

| Question | Yes | No | Response |
|---|---|---|---|
| **1. Convergence of simulations and analysis** | | | |
| 1a. Is an evaluation presented in the text to show that the property being measured has equilibrated in the simulations (*e.g.* time-course analysis)? | + | | The Methods subsections "Molecular dynamics simulations", "Ligand escape", "Agonist binding", and "Evaluation of H89 protonation state" include information about equilibration procedures. |
| 1b. Then, is it described in the text how simulations are split into equilibration and production runs and how much data were analysed from production runs? | + | | The Methods subsections "Molecular dynamics simulations", "Ligand escape", "Agonist binding", and "Evaluation of H89 protonation state" include information about how the simulations were split. |
| 1c. Are there at least 3 simulations per simulation condition with statistical analysis? | + | | Classical simulations have at least three replicas. Constant pH simulations use from 3-6 simulations per pH value to calculate the converged values for the local $pK_a$'s. τ-RAMD simulations have 100 repeats per ligand. 20 repeats were carried out for SuMD association trajectories. |
| 1d. Is evidence provided in the text that the simulation results presented are independent of initial configuration? | + | | Production runs were started from slightly different initial geometries. |
| **2. Connection to experiments** | | | |
| 2a. Are calculations provided that can connect to experiments (*e.g.* loss or gain in function from mutagenesis, binding assays, NMR chemical shifts, J-couplings, SAXS curves, interaction distances or FRET distances, structure factors, diffusion coefficients, bulk modulus and other mechanical properties, *etc*.)? | + | | Classical, association, and dissociation simulation results are discussed in relation to mutagenesis and cryo-EM data. |
| **3. Method choice** | | | |
| 3a. Do simulations contain membranes, membrane proteins, intrinsically disordered proteins, glycans, nucleic acids, polymers, or cryptic ligand binding? | + | | Simulations contain membranes and membrane proteins. Details are provided in the Methods section. |

| | | | |
|---|---|---|---|
| 3b. Is it described in the text whether the accuracy of the chosen model(s) is sufficient to address the question(s) under investigation (e.g. all-atom vs. coarse-grained models, fixed charge vs. polarizable force fields, implicit vs. explicit solvent or membrane, force field and water model, etc.)? | + | | |
| 3c. Is the timescale of the event(s) under investigation beyond the brute-force MD simulation timescale in this study that enhanced sampling methods are needed? | + | | |
| If **YES**, are the parameters and convergence criteria for the enhanced sampling method clearly stated? | + | | For association trajectories obtained using SuMD, the criteria to stop is based on the distance between binding site residues and the ligand CoM. The threshold distance is provided in the Methods subsection "Agonist binding". |
| If **NO,** is the evidence provided in the text? | ☐ | ☐ | |
| **4. Code and reproducibility** | | | |
| 4a. Is a table provided describing the system setup that includes simulation box dimensions, total number of atoms, total number of water molecules, salt concentration, lipid composition (number of molecules and type)? | | + | All this information is provided in the Methods section as text rather than a table. |
| 4b. Is it described in the text what simulation and analysis software and which versions are used? | + | | Software and their versions are provided in the Methods section. |
| 4c. Are other parameters for the system setup described in the text, such as protonation state, type of structural restraints if applied, nonbonded cutoff, thermostat and barostat, etc.? | + | | Protonation state for H89 was decided based on constant pH simulations. Unless default parameters are used, thermostat and barostat types were mentioned in the Methods section. |
| 4d. Are initial coordinate and simulation input files and a coordinate file of the final output provided as supplementary files or in a public repository? | + | | Initial coordinates and input files with an example association trajectory are provided in Zenodo (https://doi.org/10.5281/zenodo.17848900). |

| | | | | |
|---|---|---|---|---|
| 4e. Is there custom code or custom force field parameters? | | + | | |
| | If **YES**, are they provided as supplementary files or in a public repository? | + | | The original SuMD script was adjusted so that it could be applied for systems larger than 100000 atoms. It is provided in Zenodo (https://doi.org/10.5281/zenodo.17848900). |

## Supplementary References


1. Kurz M, Krett AL, Bunemann M. Voltage Dependence of Prostanoid Receptors. *Mol Pharmacol* **97**, 267-277 (2020).
2. Tao X, Zhao C, MacKinnon R. Membrane protein isolation and structure determination in cell-derived membrane vesicles. *Proc Natl Acad Sci U S A* **120**, e2302325120 (2023).
3. Kirchhofer SB*, et al.* Differential interaction patterns of opioid analgesics with micro opioid receptors correlate with ligand-specific voltage sensitivity. *Elife* **12**, (2023).
4. Punjani A, Rubinstein JL, Fleet DJ, Brubaker MA. cryoSPARC: algorithms for rapid unsupervised cryo-EM structure determination. *Nature methods* **14**, 290-296 (2017).
5. Punjani A, Zhang H, Fleet DJ. Non-uniform refinement: adaptive regularization improves single-particle cryo-EM reconstruction. *Nature methods* **17**, 1214-1221 (2020).
6. Afonine PV*, et al.* Real-space refinement in PHENIX for cryo-EM and crystallography. *Acta Crystallogr D Struct Biol* **74**, 531-544 (2018).
7. Kimanius D, Dong L, Sharov G, Nakane T, Scheres SHW. New tools for automated cryo-EM single-particle analysis in RELION-4.0. *Biochem J* **478**, 4169-4185 (2021).